

École doctorale n° 364 : Sciences Fondamentales et Appliquées

Doctorat ParisTech

THÈSE

pour obtenir le grade de docteur délivré par

l'École Nationale Supérieure des Mines de Paris

Spécialité doctorale “Science et Génie des Matériaux”

présentée et soutenue publiquement par

Ali SAAD

le xx mai 2015

NUMERICAL MODELLING OF MACROSEGREGATION INDUCED BY SOLIDIFICATION SHRINKAGE IN A LEVEL SET APPROACH

Directeurs de thèse: **Michel BELLET**
Charles-André GANDIN

Jury

M. Blablabla,	Professeur, MINES ParisTech	Rapporteur
M. Blablabla,	Professeur, Arts Et Métiers ParisTech	Rapporteur
M. Blablabla,	Chargé de recherche, ENS Cachan	Examinateur
M. Blablabla,	Danseuse, en freelance	Examinateur
M. Blablabla,	Ingénieur, MIT	Examinateur

T
H
E
S
S

Contents

1 General Introduction	1
1.1 Casting defects	2
1.2 Macrosegregation	3
1.2.1 Causes	4
1.2.2 Examples	5
1.3 Industrial Worries	7
1.4 Project context and objectives	8
1.4.1 Context	8
1.4.2 Objectives and outline	9
2 Modelling Review	13
2.1 Modelling macrosegregation	14
2.1.1 Dendritic growth	14
2.1.2 Mush permeability	14
2.1.3 Microsegregation	15
2.1.4 Macroscopic solidification model: monodomain	18
2.2 Eulerian and Lagrangian motion description	25
2.2.1 Overview	25
2.2.2 Interface capturing	26
2.3 Solidification models with level set	26
2.4 The level set method	27
2.4.1 Diffuse interface	27
2.4.2 Mixing Laws	29
2.5 Interface motion	31
2.5.1 Level set transport	31
2.5.2 Level set regularisation	32
3 Energy balance with thermodynamic tabulations	37
3.1 State of the art	38
3.2 Thermodynamic considerations	38
3.2.1 Volume averaging	38
3.2.2 The temperature-enthalpy relationship	39
3.2.3 Tabulation of properties	40

Contents

3.3	Numerical method	43
3.3.1	Enthalpy-based approach	45
3.3.2	Temperature-based approach	45
3.3.3	Convergence	46
3.4	Validation	47
3.4.1	Pure diffusion	47
3.4.2	Convection and diffusion	50
3.5	Application: multicomponent alloy solidification	53
3.5.1	Tabulations	53
3.5.2	Discussion	55
4	Macrosegregation with incompressible fluid motion	57
4.1	Introduction	58
4.2	Review fluid mechanics	58
4.3	VMS solver	58
4.4	Computational stability	58
4.4.1	CFL condition	58
4.4.2	Integration order	58
4.5	Application to multicomponent alloys	59
4.6	Macroscopic freckle prediction	59
4.6.1	Introduction	59
4.6.2	Experimental work	59
4.6.3	Macroscopic scale simulations	59
4.7	Meso-Macro freckle prediction	60
	Bibliography	61

Acronym	Standing for
ALE	Arbitrary Lagrangian-Eulerian
CCEMLCC	Chill Cooling for the Electro-Magnetic Levitator in relation with Continuous Casting of steel
CEMEF	Center for Material Forming
DLR	Deutsches Zentrum für Luft- und Raumfahrt
EML	Electromagnetic levitation
ESA	European Space Agency
FEM	Finite Element Method
ISS	International Space Station
IWT	Institut für Werkstofftechnik
LHS	Left Hand Side
MAC	Marker-and-cell
PF	Phase field
RHS	Right Hand Side
RUB	Ruhr Universität Bochum
RVE	Representative Elementary Volume
VOF	Volume Of Fluid

Contents

Chapter 1

General Introduction

Macrosegregation is a very known defect to metallurgical processes. Despite a great evolution achieved by active research during the last 60 years, it remains partially understood. Macrosegregation is often the consequence of several factors at the scale of a casting, all related to *microsegregation* happening at the scale of dendrites. Today, research in metallurgy focuses on a deeper understanding of such a connection between the different physical scales. Solidification is not only a phase change, but also a complex transformation involving small scales like nucleation, medium scales like grains growth and large scales like convection in the melt. From the nucleation theory to the mechanical behavior of metals, intricate phenomena combine to form defects in the final product. This has been seen in casting processes, such as continuous casting (fig. 1.1) and ingot casting. Surface and volume porosity, hot tearing and composition heterogeneity are known defects to the casting community. After a brief introduction of these defects, macrosegregation will be the focus of this dissertation.

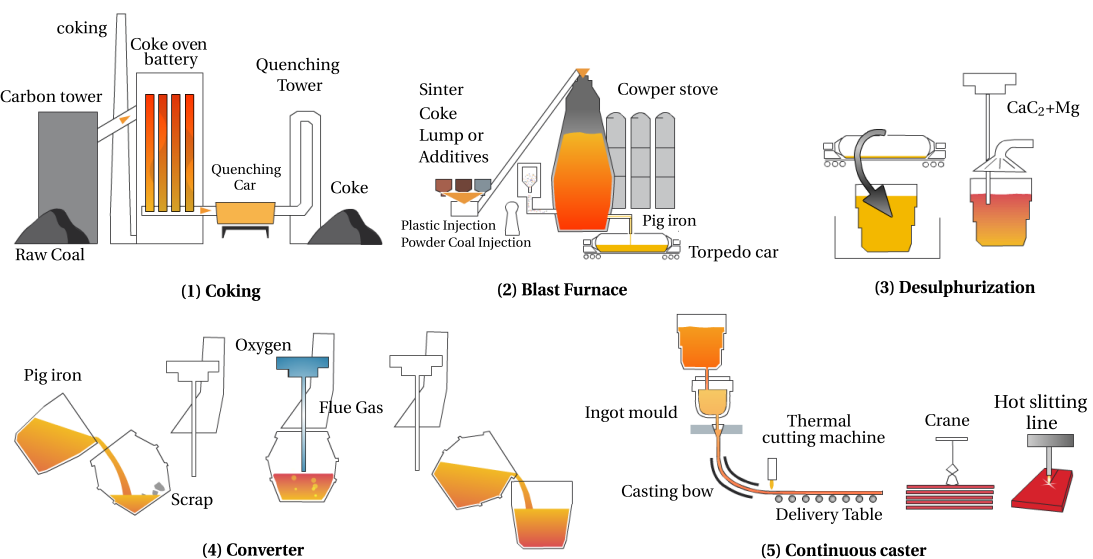


Fig. 1.1 – Main steps in a integrated steel plant

1.1 Casting defects

Undesired effects are inevitable in any industrial process. More importantly, a lot of defects in the casting industry can be disastrous in some situations where the cast product is not serviceable and hence rejected. This leads to a systematic product recycling, i.e. the product is ditched to be reheated, remelted and then cast again. From an economic point view, the operation is expensive timewise and profitwise. Understanding and preventing defects when possible, is thus crucial in the casting industry. We briefly list hereafter the main encountered defects.

Hot tearing

This defect, also denoted solidification cracking or hot cracking, occurs in the mushy zone at high solid fractions when a failure or crack appears at specific locations, the hot spots. The temperature range in which the steel is vulnerable to hot tearing is known as the brittleness temperature range (BTR). It corresponds to solid fractions greater than 90%, with the liquid phase forming a discontinuous film. Many factors can cause the failure, but the main origin is a lack of liquid feeding required to compensate for the solidification shrinkage, in the presence of thermal stresses in the mushy region. Therefore, a crack initiates then propagates in the casting, as shown in [fig. 1.2](#).



Fig. 1.2 – Crack in an aluminium slab

Porosity

Porosity is a void defect formed inside the casting or at the outer surface. It may attributed to two different factors. Firstly, we speak of *shrinkage porosity*, when a void forms as a result of density differences between the interdendritic liquid and solid network, the latter being denser than the former ([figs. 1.3c](#) and [1.3d](#)). It is basically, the same reason that initiates hot cracks. The second factor is the presence of dissolved gaseous phases in the melt ([figs. 1.3a](#) and [1.3b](#)). According to [Dantzig et al. \[2009\]](#), these gases may be initially in the melt, or created by the reaction between the metal and water found in the air or trapped in grooves at the moulds surface. If the decreasing temperature and pressure drop in the liquid are large enough, the latter becomes

supersaturated. Consequently, the nucleation of gaseous phase is triggered (just like when a cold bottle of coca-cola is opened !).



(a) Gas porosity in casting [AFS 2014].



(b) Shrinkage porosity [AFS 2014].



(c) Gas porosity in aluminium welding [WeldReality 2014].



(d) Xray of volume void inside welded duplex steel [ESAB 2014].

Fig. 1.3 – Examples of porosity in casting and welding

Freckles or segregated channels

The origin of this defect is a combined effect of microsegregation and buoyancy forces. Upon solidification, solid forms while rejecting some solute in the liquid due to partitioning (steels have a partition coefficient less than unity). When segregated solute is the lighter species, an increasing concentration in the liquid phase produces a solutal driving force inside the mushy zone, generating unstable convection currents, with "plume" shapes as often reported in the literature [Sarazin et al. 1992; Schneider et al. 1997; Shevchenko et al. 2013]. Temperature gradient is often an additional force of convection, the latter is hence qualified as "thermosolutal".

1.2 Macrosegregation

Macrosegregation generally stems from a solubility difference between a liquid phase and one or more solid phases, along with a relative velocity between these phases. While the former is responsible for local solute enrichment or depletion, the latter will propagate the composition heterogeneity on a scale much larger than just a few

Chapter 1. General Introduction

dendrites. This is why macrosegregation could be observed on the scale of a casting, up to several meters in length. While microsegregation can be healed by annealing the alloy to speed up the diffusion process and allow homogenization, heterogeneities spanning on larger distances cannot be treated after solidification. It is obvious that macrosegregation is irreversible defect. Failure to prevent it, may lead to a substantial decline in the alloy's mechanical behavior, hence its serviceability.

1.2.1 Causes

Four main factors can (simultaneously) cause fluid flow leading to macrosegregation:

Liquid dynamics

During solidification, thermal and solutal gradients result in density gradients in the liquid phase:

$$\rho^l = \rho_0^l(1 - \beta_T(T - T_0) - \sum_i \beta_{w_i^l}(w_i^l - \langle w_i \rangle_0^l)) \quad (1.1a)$$

$$\vec{\nabla} \rho^l = -\rho_0^l(\beta_T \vec{\nabla} T + \sum_i \beta_{w_i^l} \vec{\nabla} w_i^l) \quad (1.1b)$$

In eq. (1.1a), density is assumed to vary linearly with temperature and phase composition for each chemical species (index i). The slopes defining such variations are respectively the thermal expansion coefficient β_T and the solutal expansion coefficients $\beta_{w_i^l}$, given by:

$$\beta_T = -\frac{1}{\rho_0^l} \left(\frac{\partial \rho^l}{\partial T} \right) \quad (1.2a)$$

$$\beta_{w_i^l} = -\frac{1}{\rho_0^l} \left(\frac{\partial \rho^l}{\partial w_i^l} \right) \quad (1.2b)$$

The linear fit assumes also that the density takes a reference value, ρ_0^l , when temperature and liquid composition reach reference values, respectively T_0 and $\langle w_i \rangle_0^l$, while the coefficients $\beta_{w_i^l}$ remain constant. However, in some situations, a suitable thermodynamic database providing accurate density values is far better than a linear fit, especially in the current context of macrosegregation. Such possibility will be discussed later in the manuscript (cf. SECTION TODO)

In the presence of gravity, the density gradient in eq. (1.1b), causes thermosolutal convection in the liquid bulk and a subsequent macrosegregation.

Solidification shrinkage

Solid alloys generally have a greater density than the liquid phase ($\rho^s > \rho^l$), thus occupy less volume, with the exception of silicon where the opposite is true. Upon

solidification, the liquid moves towards the solidification front to compensate for the volume difference caused by the phase change, as well as the thermal contraction. When macrosegregation is triggered by solidification shrinkage, we speak of *inverse segregation*: while one would naturally expect negative macrosegregation in areas where solidification begins and positive inside the alloy, shrinkage promotes the opposite phenomenon, by bringing solute-richer liquid towards the solidifying areas, thus raising their solute content, and resulting in a positively segregated solid. In contrast to liquid convection, shrinkage flow may cause macrosegregation even without gravity.

Movement of equiaxed grains

Equiaxed grains can grow in the liquid bulk where thermal gradients are weak, or in the presence of inoculants. Consequently, they are transported by the flow (floating or sedimenting, depending on their density [Beckermann 2002]) which leads to negative macrosegregation in their final position.

Solid deformation

Stresses of thermal and mechanical nature are always found in casting processes (e.g. bulging between rolls in continuous casting). Deformation of the semi-solid in the mushy zone causes a relative solid-liquid flow in the inward (tensile stresses) or outward (compressive stresses) direction, causing macrosegregation.

1.2.2 Examples

In continuous casting

The partially solidified slab is carried through a series of rolls that exert contact forces to straighten it. As the mushy part of a slab enters through these rolls, interdendritic liquid is expelled backwards, i.e. regions with lower solid fraction. Since the boundaries solidify earlier than the centre, the enriched liquid accumulates halfway in thickness, forming a centreline macrosegregation as shown in [fig. 1.4](#). Other types of segregates (channels, A-segregates ...) can also be found but remain more specific to ingot casting.

In ingot casting

A variety of segregation patterns can be encountered in heavy ingots:

- the lower part is characterized by a negative segregation cone promoted by the sedimentation of equiaxed crystals,
- positive segregation channels, known as A-segregates, form along the columnar dendritic zones, close to the vertical contact with the mould,

Chapter 1. General Introduction

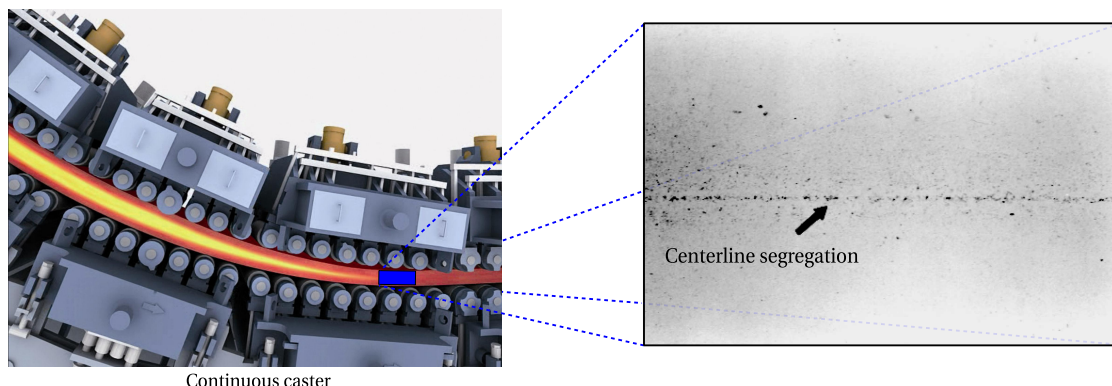


Fig. 1.4 – Centreline segregation in a steel slab [Beckermann 2002]

- positive V-segregates can be identified in the centre of the ingot,
- a positive macrosegregation in the upper zone where the last liquid solidifies, the so-called "hot-top", caused by solidification shrinkage (inverse segregation) and thermosolutal buoyancy forces.

Combeau et al. [2009] state that A-segregates and V-segregates formation is mainly attributed to local flow phenomena. As such, their scale is finer than macrosegregation, hence called "mesosegregates".

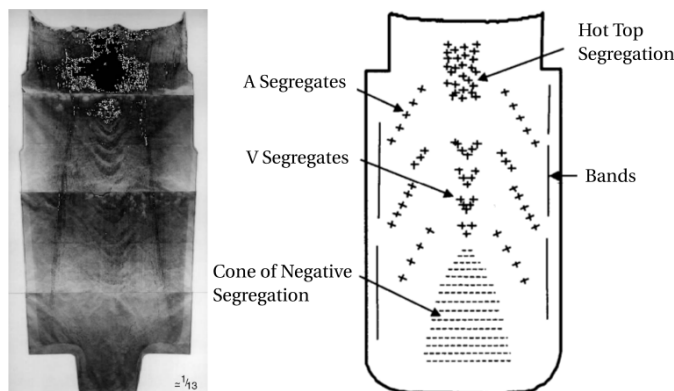
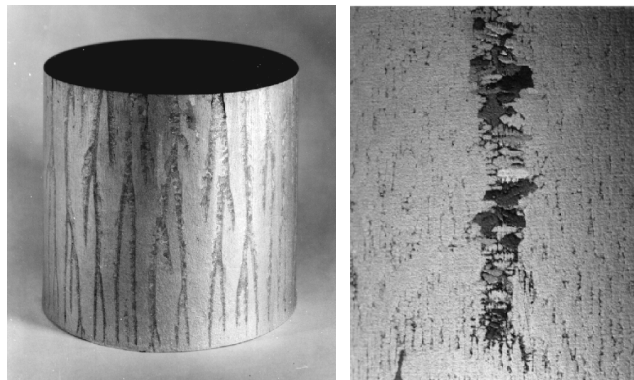


Fig. 1.5 – Sulphur print (left) of a 65-ton steel ingot [Lesoult 2005] showing various patterns (right) of macrosegregation [Flemings 1974]

In investment casting

This process is widely used to cast single-crystal (SC) alloys for turbines and other applications that require excellent mechanical behavior [Giamei et al. 1970]. When performed by directional solidification, thermosolutal forces thrust segregated species outside of the mushy zone into the liquid bulk. The segregation scale ranges from a few dendrites to a few hundreds of them, hence forming "long and narrow trails" (fig. 1.6a) as described by Felicelli et al. [1991]. Freckles are frequently formed by small equiaxed

grains ([fig. 1.6b](#)), probably caused by a uniform temperature gradient that settles as the channels become richer in solute. They can be observed on the ingot's surface, as well as in the volume.



(a) Small cylinder ingot showing freckles on the outer surface

(b) Zoomed image showing the microstructure in one freckle

Fig. 1.6 – Freckles in directional casting of nickel-base superalloys

1.3 Industrial Worries

Steel production has continuously increased over the years to meet the industrial needs. [Figure 1.7](#) shows this increase between 1980 and 2013 with a clear dominance of the Chinese production. Quality constraints have also increased where specific grades of steel are needed in critical applications such as mega-structures in construction and heavy machinery. Therefore, alloys with defects are considered vulnerable and should be avoided as much as possible during the casting process. As such, steelmakers have been investing in research, with the aim of understanding better the phenomena leading to casting problems, and improve the processes when possible.

Simulation software dedicated to alloy casting is one of the main research investments undertaken by steelmakers. These tools coming from academic research are actively used to optimize the process. However, few are the tools that take into account the casting environment. For instance, the continuous casting process, in [fig. 1.1](#), is a chain process where the last steps involve rolls, water sprays and other components. A dedicated software is one that can provide the geometric requirements with suitable meshing capabilities, as well as respond to metallurgical and mechanical requirements, mainly:

- handling moulds and their interaction with the alloy (thermal resistances ...)
- handling alloy filling and predicting velocity in the liquid and mushy zone
- handling thermomechanical stresses in the solid

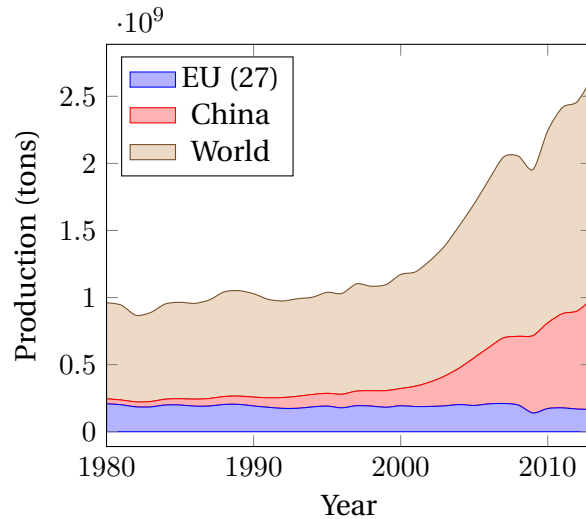


Fig. 1.7 – Evolution curves of crude steel worldwide production from 1980 to 2013 [WSA 2014].

- handling multicomponent alloys and predicting macrosegregation
- handling finite solute diffusion in solid phases
- handling real alloy properties (not just constant thermophysical/thermomechanical properties)

1.4 Project context and objectives

1.4.1 Context

The European Space Agency (ESA) has been actively committed, since its foundation in 1975, in the research field. Its covers not only exclusive space applications, but also fundamental science like solidification. This thesis takes part of the ESA project entitled *CCEMLCC*, abbreviating "Chill Cooling for the Electro-Magnetic Levitator in relation with Continuous Casting of steel". The three-year contract from 2011 to late 2014 denoted *CCEMLCC II*, was preceded by an initial project phase, *CCEMLCC I*, from 2007 to 2009. The main focus is studying containerless solidification of steel under microgravity conditions. A chill plate is later used to extract heat from the alloy, simulating the contact effect with a mould in continuous casting or ingot casting. A partnership of 7 industrial and academic entities was formed in *CCEMLCC II*. Here is a brief summary of each partner's commitment:

Academic partners

- CEMEF (France): numerical modelling of microgravity chill cooling experiments
- DLR (German Aerospace Centre) and RUB university (Germany): preparation of a chill cooling device for electromagnetic levitation (EML), microgravity testing

and investigation of growth kinetics in chill-cooled and undercooled steel alloys

- University of Alberta (Canada): impulse atomization of the D2 tool steel
- University of Bremen - IWT institute (Germany): study of melt solidification in atomization processing

Industrial partners

- ARCELORMITTAL (France): elaboration of a series of steel grades used in microgravity and ground studies
- METSO Minerals Inc. (Finland): material production with D2 tool steel for spray forming
- TRANSVALOR (France): development and marketing of casting simulation software *Thercast*®

CEMEF, as an academic partner, contributed to the work by proposing numerical models in view of predicting the chill cooling of steel droplets. A first model was developed by [Rivaux \[2011\]](#) whereas the present thesis discusses a new model. The experimental work considered various facilities and environments to set a droplet of molten alloy in levitation: EML ([fig. 1.8](#)) for ground-based experiments, microgravity in parabolic flight or sounding rockets and last, microgravity condition on-board the International Space Station (ISS)



Fig. 1.8 – Electromagnetic levitation [[DLR 2014](#)].

1.4.2 Objectives and outline

The main focus of the present thesis is predicting macrosegregation with liquid dynamics assuming a fixed solid phase, i.e. no account of solid transport (e.g. equiaxed crystals sedimentation) and no account of solid deformation. In CEMEF, this scope has been adopted for previous work by [Gouttebroze \[2005\]](#), [Liu \[2005\]](#), [Mosbah \[2008\]](#), [Rivaux \[2011\]](#), and [Carozzani \[2012\]](#). Nevertheless, many modelling features evolved with time such as going from two-dimensional to three-dimensional modelling, resolution schemes for each of the conservation equations: energy, chemical species and liquid momentum, Eulerian or Lagrangian descriptions, modelling of grain structure and others. In this thesis, we propose a numerical model that takes into account i) the energy conservation in a temperature formulation based on a thermodynamic

Chapter 1. General Introduction

database mapping, ii) the liquid momentum conservation with thermosolutal convection and solidification shrinkage as driving forces, iii) solute mass conservation and iv) solidification paths at full equilibrium for multicomponent alloys microsegregation. Moreover, all equations are formulated in a pure Eulerian description while using the Level Set method to keep implicitly track of the interface between the alloy and surrounding gas. To the author's knowledge, this work combining macrosegregation prediction using the level set methodology to track the metal-air interface during shrinkage has no precedent in casting and solidification literature. The model couples in a weak fashion, all four conservation equations presented in [fig. 1.9](#), showing on the one hand, that microsegregation is an essential common link between these equations, while on the other hand, the level set interacts with conservations equations by giving the interface position.

Numerical tools: Cimlib relying on PETSc, parallelized with MPICH2, paraview and python as tools for postprocess and analysis.

The previously mentionned simulation requirements are not met in a single casting software package. Nevertheless, *Thercast[®]* is a promising tool that already handles a part of the above points. The current thesis developments are done using C++ language as a part of the in-house code, known as *CimLib* [[Digonnet et al. 2007](#); [Mesri et al. 2009](#)]. This fully parallel library is the main academic research support for *Thercast[®]*

Outline: each chapter content ...

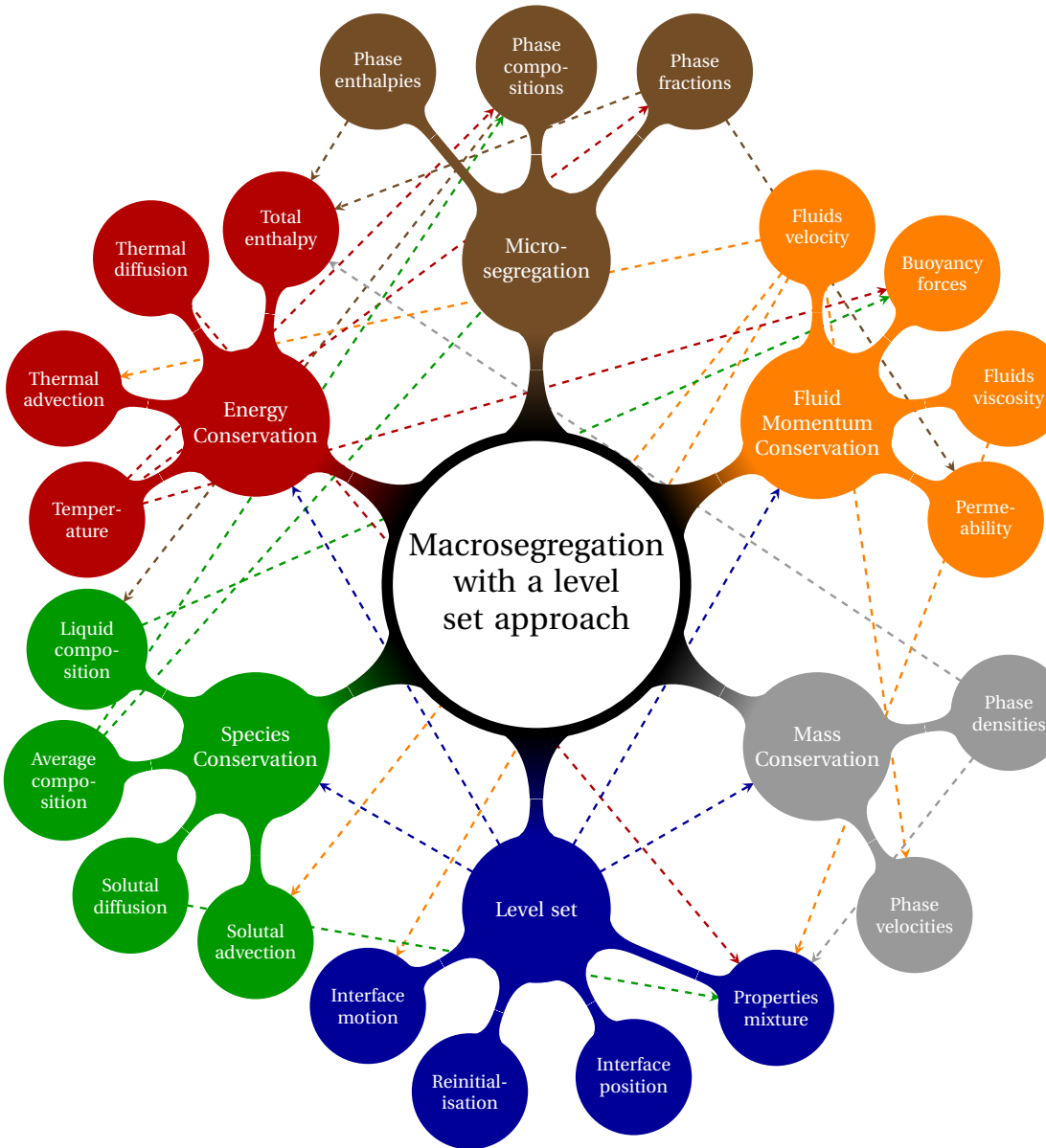


Fig. 1.9 – A graphical representation of the main ingredients of the macrosegregation model with the level set methodology when no solid deformation or movement are considered. The dashed lines represent the possible interaction between the components.

Chapter 1. General Introduction

Chapter 2

Modelling Review

Contents

2.1	Modelling macrosegregation	14
2.1.1	Dendritic growth	14
2.1.2	Mush permeability	14
2.1.3	Microsegregation	15
2.1.4	Macroscopic solidification model: monodomain	18
2.2	Eulerian and Lagrangian motion description	25
2.2.1	Overview	25
2.2.2	Interface capturing	26
2.3	Solidification models with level set	26
2.4	The level set method	27
2.4.1	Diffuse interface	27
2.4.2	Mixing Laws	29
2.5	Interface motion	31
2.5.1	Level set transport	31
2.5.2	Level set regularisation	32

2.1 Modelling macrosegregation

2.1.1 Dendritic growth

In a casting process, the chill surface i.e. the contact between the molten alloy and relatively cold moulds, is the first area to solidify. Thermal gradient, G , and cooling rate R are two crucial process parameters that define the interface speed \vec{v}^* , which in turn, affects the initial microstructure. Although it may be not easy to control them, it remains important to understand their implication in solidification.

The solid-liquid interface fluctuates when solidifying, thus perturbations may appear on the front, locally destabilizing it. Two outcome scenarios are possible. The first scenario is characterized by low values of \vec{v}^* where the interface maintains a planar shape, hence we speak of *planar growth*. With this kind of growth, a random protuberance appearing at the interface, has a low tip velocity (low driving force of solidification). As such, the rest of the interface catches up, keeping the planar geometry. In another scenario, where a real casting is considered, the interface speed is greater in general, due to high solidification rate. The protuberance tip will be pulled into a liquid less rich in solute than the interface. The zone ahead of the solid-liquid interface is constitutionally undercooled [Tiller et al. 1953], giving a greater driving force for the protuberance to grow in the direction of the thermal gradient. As it has a tree-like shape, we speak of *dendritic growth*. Near the chill surface, dendrites are columnar, with a favourable growth in the $<100>$ direction for alloys with cubic lattices, but different orientations are also reported in the literature [see Dantzig et al. 2009, p. 289]. If temperature is uniform, which is the case usually far from mould walls, a similar dendritic growth phenomenon occurs, but with an equiaxed morphology.

Columnar dendrites are characterized by a primary spacing, λ_1 , between the main trunks, and a secondary spacing, λ_2 , for the arms that are perpendicular to the trunks. It should be noted that λ_2 , together with the grain size, are two important microstructural parameters in the as-cast microstructure [Easton et al. 2011]. Further branching may occur but will not be discussed here.

2.1.2 Mush permeability

The dendritic geometry is crucial in solidification theory as it exhibits lower solid fraction compared to a microstructure formed by planar growth. This fact has consequences on the fluid-structure interaction in the mushy zone, namely the liquid flow through dendrites. At the chill surface, the solid grows gradually from dispersed growing nuclei to a permeable solid skeleton, until finally grains have fully grown at the end of phase change. The intermediate state where liquid can flow in and out of the mushy zone through the dendrites is a key phenomenon from a rheological perspective. The flow through the solid skeleton is damped by primary and secondary dendrites, resulting in momentum dissipation just like in saturated porous media. The famous Darcy [1856] law relates the pressure gradient ($\vec{\nabla}p$) to the fluid velocity \vec{v} ,

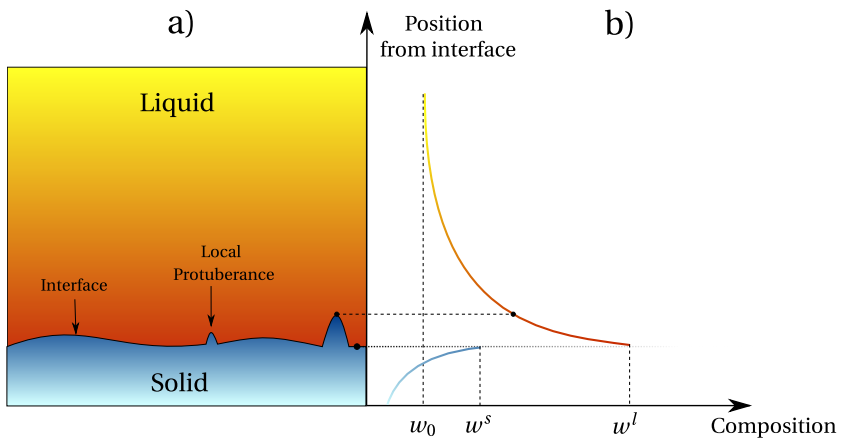


Fig. 2.1 – Schematic of a) a protuberance growing on the solid-liquid interface with b) the corresponding composition profiles (Reproduced and adapted from DoITPoMS [2000], © DoITPoMS, University of Cambridge).

through the following equation [Rappaz et al. 2003]:

$$\vec{v} = \frac{\mathbb{K}}{\mu^l} \vec{\nabla} p \quad (2.1)$$

where μ^l is the liquid dynamic viscosity and \mathbb{K} is the permeability tensor. The latter parameter has been the subject of numerous studies that aimed to predict it from various microstructural or morphological parameters. Some of these studies have started even before the first attempts to model macrosegregation by Flemings et al. [1967], Flemings et al. [1968a], and Flemings et al. [1968b]. Basically, all models include the solid fraction, g^s , as input to predict mush permeability along with empirical data. An instance of such models is the work of Xu et al. [1991]. Some models rely additionally on the primary dendrite arm spacing λ_1 like Blake-Kozeny [Ramirez et al. 2003], or the secondary dendrite arm spacing λ_2 like Carman-Kozeny, as a meaningful parameter to determine an isotropic permeability. Other models like Poirier [1987] and Felicelli et al. [1991] derive an anisotropic permeability based on both λ_1 and λ_2 .

The present work uses Carman-Kozeny as a constitutive model for the isotropic permeability scalar (zero order tensor):

$$\mathbb{K} = \frac{\lambda_2^2 g^l{}^3}{180 (1 - g^l)^2} \quad (2.2)$$

2.1.3 Microsegregation

Microsegregation is a fundamental phenomenon in solidification. The simplest definition is an uneven distribution of solute between the liquid and the herein growing solid, at the microscopic scale of the interface separating these phases. If we consider a binary alloy, then the solubility limit is the key factor that dictates the composition

at which a primary solid phase exists in equilibrium. The segregation (or partition) coefficient k determines the extent of solute rejection into the liquid during solidification:

$$k = \frac{w^{s^*}}{w^{l^*}} \quad (2.3)$$

where w^{s^*} and w^{l^*} are the compositions of the solid and liquid respectively, at the interface. When the segregation coefficient is less than unity (such is the case for most alloys during dendritic solidification), the first solid forms with a composition $w^{s^*} = kw^{l^*} = kw_0$ less than the liquid's composition w_0 , the latter being initially at the nominal composition, w_0 . Figure 2.2 illustrates a typical binary phase diagram where the real solidus and liquidus are represented by solid lines, while the corresponding linear approximations are in grey dashed lines. For most binary alloys, this linearisation simplifies derivation of microsegregation models, as k becomes independent of temperature.

For each phase, the relationship between the composition at the interface and that in the bulk depends on the chemical homogenisation ability of the phase. The more homogeneous a phase, the closer the concentrations between the interface and the bulk, hence closer to equilibrium. It is thus essential to study the effect of homogenisation on the segregation behaviour and the subsequent effect on solidification, which leads the formalism of microsegregation models.

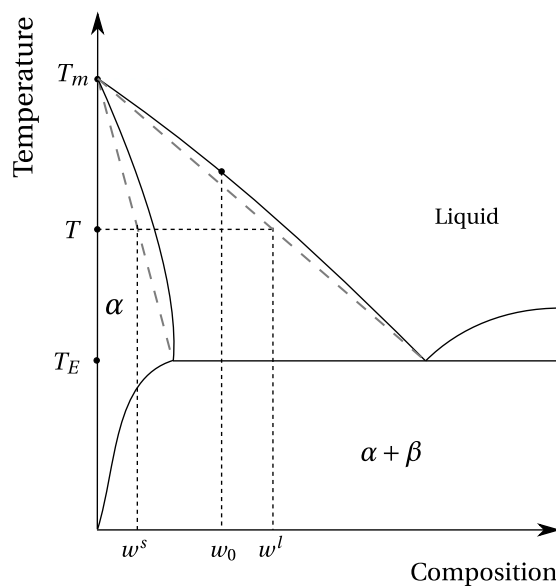


Fig. 2.2 – Typical eutectic phase diagram of a binary alloy showing the real solidus and liquidus at full equilibrium, with the corresponding linear approximations (grey dashed lines). T_m and T_E are respectively the melting point of the solvent and the eutectic temperature.

Microsegregation models

Solid formation depends greatly on the ability of chemicals species to diffuse within each of the solid and liquid phases, but also across the solid-liquid interface. Furthermore, chemical diffusion like all other diffusional process, is a time-dependent phenomenon. One can thus conclude that two factors influence the amount of solid formation: cooling rate and diffusion coefficients. However, convection and other mechanical mixing sources, homogenise the composition much faster than atomic diffusion. As such, *complete mixing* in the liquid is always an acceptable assumption, regardless of the solidification time. We may speak of infinite diffusion in the liquid. Nevertheless, diffusion in the solid, also known as *back diffusion*, is the only transport mechanism with very low diffusion coefficients. Therefore, chemical species require a long time, i.e. low cooling rate, to completely diffuse within the solid. The difference in diffusional behaviour at the scale of a secondary dendrite arms, is summarized by two limiting segregation models of perfect equilibrium and nonequilibrium, which are the lever rule and Gulliver-Scheil models, respectively. Afterwards, models with finite back diffusion are presented.

Lever rule

The lever rule considers an ideal equilibrium in all phases, i.e. solidification is extremely slow, hence phase compositions are homogeneous ($w^{l^*} = w^l$ and $w^{s^*} = w^s$) at all times as a consequence of complete mixing. These compositions are given by:

$$w^l = w^{l^*} = kw^{s^*} = kw^s \quad (2.4)$$

$$w^s = w^{s^*} = \frac{w_0}{k(1 - f^s) + f^s} \quad (2.5)$$

At the end of solidification, the composition of the solid phase is equal to the nominal composition, $w^s = w_0$

Gulliver-Scheil

The other limiting case is the absence of diffusion in the solid. That includes also the diffusion at the interface, so nothing diffuses in or out. The consequence is a steady increase of the homogeneous liquid composition while the solid composition remains non-uniform. Compared to a full equilibrium approach, higher fractions of liquid will remain until eutectic composition is reached, triggering a eutectic solidification. The phase compositions are given by:

$$w^l = w^{l^*} = kw^{s^*} \quad (2.6)$$

$$w^s = kw_0(1 - f^s)^{1-k} \quad (2.7)$$

Finite back diffusion

It has been concluded that the assumption of a negligible back diffusion overestimates the liquid composition and the resulting eutectic fraction. Therefore, many models studied the limited diffusion in the solid. One of the earliest models is the Brody-Flemings models [Khan et al. 2014] that is based on a differential solute balance equation for a parabolic growth rate, as follows:

$$w^l = w^{l*} = kw^{s*} \quad (2.8)$$

$$w^s = kw_0 [1 - (1 - 2\text{Fo}^s k) f^s]^{\frac{k-1}{1-2\text{Fo}^s k}} \quad (2.9)$$

where Fo^s is the dimensionless *Fourier number* for diffusion in the solid [Dantzig et al. 2009]. It depends on the solid diffusion coefficient D^s , solidification time t_s and the secondary dendrite arm spacing, as follows:

$$\text{Fo}^s = \frac{D^s t_s}{(\lambda_2/2)^2} \quad (2.10)$$

Several other models were since suggested and used. The interested reader is referred to the following non exhaustive list of publications: Clyne et al. [1981], Kobayashi [1988], Ni et al. [1991], Wang et al. [1993], Combeau et al. [1996], Martorano et al. [2003], and Tourret et al. [2009]. It is noted that some of these publications consider also a finite diffusion in the liquid phase.

2.1.4 Macroscopic solidification model: monodomain

In this section, we will present the macroscopic conservations equations that enable us to predict macrosegregation in the metal when the latter is the only domain in the system.

Volume averaging

It is crucial for a solidification model to represent phenomena on the microscale, then scale up to predict macroscopic phenomena. Nevertheless, the characteristic length of a small scale in solidification may represent a dendrite arm spacing, for instance the mushy zone permeability, as it may also represent an atomic distance if one is interested, for instance, in the growth competition between diffusion and surface energy of the solid-liquid interface. Modelling infinitely small-scale phenomena could be prohibitively expensive in computation time, if we target industrial scales.

The volume averaging is a technique that allows bypassing this barrier by averaging small-scale variations on a so-called *representative volume element* (RVE) [Dantzig et al. 2009] of volume V_E , with the following dimensional constraints: the element should be large enough to "see" and average microscopic fluctuations whilst being smaller than the scale of macroscopic variations. Solid and liquid may exist simultaneously in

the RVE, but no gas phase is considered (volume saturation: $V^s + V^l = V_E$). Moreover, temperature is assumed uniform and equal for all the phases. The formalism, introduced by Ni et al. [1991], is summarized by the following equations for any physical quantity ψ :

$$\langle \psi \rangle = \frac{1}{V_E} \int_{V_E} \psi \, d\Omega = \langle \psi^s \rangle + \langle \psi^l \rangle \quad (2.11)$$

where $\langle \psi \rangle^s$ and $\langle \psi \rangle^l$ are phase averages of ψ . Then, for any phase ϕ , one can introduce the *phase intrinsic average* of ψ , denoted $\langle \psi \rangle^\phi$, by writing:

$$\langle \psi^\phi \rangle = \frac{1}{V_E} \int_{V^\phi} \psi \, d\Omega = g^\phi \langle \psi \rangle^\phi \quad (2.12)$$

where g^ϕ is the volume fraction of the phase. To finalize, the averaging is applied to temporal and spatial derivation operators [Rivaux 2011]:

$$\langle \frac{\partial \psi^\phi}{\partial t} \rangle = \frac{\partial \langle \psi^\phi \rangle}{\partial t} - \int_{\Gamma^*} \psi^\phi \vec{v}^* \cdot \vec{n}^\phi \, dA \quad (2.13)$$

$$\langle \vec{\nabla} \psi^\phi \rangle = \vec{\nabla} \langle \psi^\phi \rangle + \int_{\Gamma^*} \psi^\phi \vec{n}^\phi \, dA \quad (2.14)$$

where \vec{v}^* is the local relative interface velocity and Γ^* is the solid-liquid interface, while \vec{n}^ϕ is the normal to Γ^* , directed outwards. The surface integral term in eqs. (2.13) and (2.14) is an *interfacial average* that expresses exchanges between the phases across the interface. The previous equations will be used to derive a set macroscopic conservation equations. It is noted that the intrinsic average $\langle \psi \rangle^\phi$ may be replaced by ψ^ϕ for notation simplicity, whenever the averaging technique applies.

Macroscopic equations

A monodomain macroscopic model relies on four main conservation equations to predict macrosegregation in a single alloy domain, i.e. the latter is considered without any interaction with another alloy or ambient air. The general form of a conservation equation of any physical quantity ψ is given by [Rappaz et al. 2003]:

$$\frac{\partial \psi}{\partial t} + \nabla \cdot (\psi \vec{v}) - \nabla \cdot \vec{j}_\psi = Q_\psi \quad (2.15)$$

The first LHS term in eq. (2.15) represents the time variation of ψ , the second term accounts for transport by advection while the third is the diffusive transport and the RHS term represents a volume source. The considered equations are mass, energy, liquid momentum and species conservation, all summarized in table 2.1. The solid momentum is not considered as we assume a fixed and rigid solid phase ($\vec{v}^s = \vec{0}$). We

Chapter 2. Modelling Review

Table 2.1 – Summary of conservation equations with their variables.

Conservation Equation	ψ	\vec{j}_ψ	Q_ψ
Mass	$\langle \rho \rangle$	—	—
Energy	$\langle \rho h \rangle$	$\langle \vec{q} \rangle$	—
Species	$\langle \rho w_i \rangle$	$\langle \vec{j}_i \rangle$	—
Liquid momentum	$\langle \rho \vec{v}^l \rangle$	$-\langle \overline{\vec{\sigma}^l} \rangle$	\vec{F}_v^l

develop the ingredients of these equations using the averaging technique, as follows:

$$\langle \rho \rangle = g^l \rho^l + g^s \rho^s \quad (2.16)$$

$$\langle \rho \vec{v} \rangle = g^l \rho^l \vec{v}^l + g^s \rho^s \vec{v}^s \quad (2.17)$$

$$\langle \rho h \rangle = g^l \rho^l h^l + g^s \rho^s h^s \quad (2.18)$$

$$\langle \rho h \vec{v} \rangle = g^l \rho^l h^l \vec{v}^l + g^s \rho^s h^s \vec{v}^s \quad (2.19)$$

$$\langle \rho w_i \rangle = g^l \rho^l w_i^l + g^s \rho^s w_i^s \quad (2.20)$$

$$\langle \rho w_i \vec{v} \rangle = g^l \rho^l w_i^l \vec{v}^l + g^s \rho^s w_i^s \vec{v}^s \quad (2.21)$$

Next, we define the average diffusive fluxes, \vec{q} for energy and \vec{j}_i for solutes, using Fourier's conduction law and Fick's first law, respectively:

$$\langle \vec{q} \rangle = -g^l \langle \kappa^l \rangle \vec{\nabla} T - g^s \langle \kappa^s \rangle \vec{\nabla} T \quad (2.22)$$

$$\langle \vec{j}_i \rangle = -g^l D^l \vec{\nabla} w_i^l - g^s D^s \vec{\nabla} w_i^s \quad (2.23)$$

In eq. (2.23), the solid diffusion coefficient is neglected, by considering that for macroscopic scales, the average composition of the alloy is much more influenced by advective and diffusive transport in the liquid. In eq. (2.22), we assumed that phases are at thermal equilibrium, that is, temperature is uniform in the RVE.

Now that the main conservation equations ingredients are properly defined, we may write each averaged conservation equations as the sum of two local conservation equations for each phase in the RVE, hence introducing also interfacial average terms. For instance, the local mass balance in each phase is given by:

$$\frac{\partial}{\partial t} (g^l \rho^l) + \nabla \cdot (g^l \rho^l \vec{v}^l) = S_V \langle \rho^l \vec{v}^{l*} \cdot \vec{n} \rangle^* - S_V \langle \rho^l \vec{v}^* \cdot \vec{n} \rangle^* \quad (2.24a)$$

$$\frac{\partial}{\partial t} (g^s \rho^s) + \nabla \cdot (g^s \rho^s \vec{v}^s) = -S_V \langle \rho^s \vec{v}^{s*} \cdot \vec{n} \rangle^* + S_V \langle \rho^s \vec{v}^* \cdot \vec{n} \rangle^* \quad (2.24b)$$

where $S_V = A_{sl}/V_E$ is the specific surface area, \vec{v}^{l*} and \vec{v}^{s*} are respectively, the liquid and solid phase velocity at the interface and \vec{v}^* is the previously introduced solid-liquid interface velocity. For instance, the first interfacial exchange term in the RHS of

eq. (2.24a) is expanded as follows [Dantzig et al. 2009]:

$$S_V \langle \rho^l \vec{v}^{l*} \cdot \vec{n} \rangle^* = \frac{A_{sl}}{V_E} \left(\frac{1}{A_{sl}} \int_{A_{sl}} \rho^l \vec{v}^{l*} \cdot \vec{n} \, dA \right) \quad (2.25a)$$

$$= \frac{1}{V_E} \int_{A_{sl}} \rho^l \vec{v}^{l*} \cdot \vec{n} \, dA \quad (2.25b)$$

Summing equations (2.24a) and (2.24b), results in the overall mass balance in the RVE:

$$\begin{aligned} \frac{\partial}{\partial t} \left(g^l \rho^l + g^s \rho^s \right) + \nabla \cdot \left(g^l \rho^l \vec{v}^l + g^s \rho^s \vec{v}^s \right) = \\ S_V \langle \rho^l \left(\vec{v}^{l*} - \vec{v}^* \right) \cdot \vec{n} \rangle^* - S_V \langle \rho^s \left(\vec{v}^{s*} - \vec{v}^* \right) \cdot \vec{n} \rangle^* \end{aligned} \quad (2.26)$$

where the RHS cancels to zero as shown by Ni et al. [1991]. Moreover, the authors show that with their averaging technique, interfacial exchanges for energy, chemical species and momentum cancel out as they are equal in absolute value but opposite in sign. Using eqs. (2.16) to (2.23) and following the same procedure done in eq. (2.26), the averaged mass balance hence writes:

$$\frac{\partial \langle \rho \rangle}{\partial t} + \nabla \cdot \langle \rho \vec{v} \rangle = 0 \quad (2.27)$$

whereas the averaged energy balance writes:

$$\frac{\partial \langle \rho h \rangle}{\partial t} + \nabla \cdot \langle \rho h \vec{v} \rangle - \nabla \cdot \left(\langle \kappa \rangle \vec{\nabla} T \right) = 0 \quad (2.28)$$

and finally the species balance writes:

$$\frac{\partial \langle \rho w_i \rangle}{\partial t} + \nabla \cdot \langle \rho w_i \vec{v} \rangle - \nabla \cdot \left(g^l D^l \vec{\nabla} \left(\rho^l w_i^l \right) \right) = 0 \quad (2.29)$$

As stated previously, the momentum balance in the solid phase is not taken into consideration, hence we do not sum the corresponding local conservation equations. This has consequences on the advection terms in energy and species conservation, and later on we will show the consequences on the momentum conservation in the liquid. First, the advection terms in eqs. (2.28) and (2.29) shall be redefined by considering that the fluid is incompressible ($\nabla \cdot \langle \vec{v}^l \rangle = 0$), which yields:

$$\nabla \cdot \langle \rho h \vec{v} \rangle = \langle \vec{v}^l \rangle \cdot \vec{\nabla} \left(\rho^l h^l \right) \quad (2.30)$$

$$\nabla \cdot \langle \rho w_i \vec{v} \rangle = \langle \vec{v}^l \rangle \cdot \vec{\nabla} \left(\rho^l w_i^l \right) \quad (2.31)$$

As for the liquid momentum balance, we write:

$$\frac{\partial}{\partial t} \left(\rho^l g^l \vec{v}^l \right) + \vec{\nabla} \cdot \left(\rho^l g^l \vec{v}^l \times \vec{v}^l \right) = \vec{\nabla} \cdot \left(g^l \bar{\bar{\sigma}}^l \right) + g^l \vec{F}_v^l + \vec{\Gamma}^l \quad (2.32)$$

where \vec{F}_v^l is the vector of external body forces exerted on the liquid phase. In our case, it accounts for the fluid's weight:

$$\vec{F}_v^l = \rho^l \vec{g} \quad (2.33)$$

The interfacial momentum transfer between the solid and liquid phases in [eq. \(2.32\)](#) is modelled by a momentum flux vector $\vec{\Gamma}^l$, consisting of hydrostatic and deviatoric parts, such that:

$$\vec{\Gamma}^l = \vec{\Gamma}_p^l + \vec{\Gamma}_{\mathbb{S}}^l \quad (2.34)$$

$$\vec{\Gamma}_p^l = p^{l*} \vec{\nabla} g^l = p^l \vec{\nabla} g^l \quad (2.35)$$

$$\vec{\Gamma}_{\mathbb{S}}^l = -g^{l2} \mu^l \mathbb{K}^{-1} \left(\vec{v}^l - \vec{x}^s \right) \quad (2.36)$$

where p^{l*} is the pressure at the interface, considered to be equal to the liquid hydrostatic pressure p^l , \mathbb{K} is a permeability scalar (isotropic) computed using [eq. \(2.1\)](#) and μ^l is the liquid's dynamic viscosity. The general form of the Cauchy liquid stress tensor in [eq. \(2.32\)](#) is decomposed as follows:

$$\langle \bar{\bar{\sigma}}^l \rangle = g^l \bar{\bar{\sigma}}^l = - \left(\langle p^l \rangle - \lambda \nabla \cdot \langle \vec{v}^l \rangle \right) \bar{\bar{\mathbf{I}}} + \langle \bar{\bar{\mathbb{S}}}^l \rangle \quad (2.37)$$

where λ is a dilatational viscosity [[Dantzig et al. 2009](#)] and $\bar{\bar{\mathbb{S}}}^l$ is the liquid strain deviator tensor. In the literature, the coefficient λ is taken proportional to the viscosity: $\lambda = \frac{2}{3} \mu^l$. However, as we consider an incompressible flow, the divergence term vanishes, thus rewriting [eq. \(2.37\)](#) as follows:

$$\langle \bar{\bar{\sigma}}^l \rangle = -\langle p^l \rangle \bar{\bar{\mathbf{I}}} + \langle \bar{\bar{\mathbb{S}}}^l \rangle \quad (2.38a)$$

$$\langle \bar{\bar{\sigma}}^l \rangle = -\langle p^l \rangle \bar{\bar{\mathbf{I}}} + 2\mu^l \langle \dot{\bar{\bar{\mathbb{S}}}^l} \rangle \quad (2.38b)$$

where the transition from [eq. \(2.38a\)](#) to [eq. \(2.38b\)](#) is made possible by assuming a Newtonian behaviour for the liquid phase. The strain rate tensor, $\langle \dot{\bar{\bar{\mathbb{S}}}^l} \rangle$, depends on the average liquid velocity:

$$\langle \dot{\bar{\bar{\mathbb{S}}}^l} \rangle = \frac{1}{2} \left(\bar{\bar{\nabla}} \langle \vec{v}^l \rangle + \bar{\bar{\nabla}}^t \langle \vec{v}^l \rangle \right) \quad (2.39)$$

Finally, we obtain the final form of momentum conservation in the liquid phase coupled with the averaged mass balance, by injecting [eqs. \(2.33\), \(2.35\), \(2.36\), \(2.38b\)](#)

and (2.39) in eq. (2.32):

$$\frac{\partial}{\partial t} \left(\rho^l \langle \vec{v}^l \rangle \right) + \frac{1}{g^l} \vec{\nabla} \cdot \left(\rho^l \langle \vec{v}^l \rangle \times \langle \vec{v}^l \rangle \right) = - g^l \vec{\nabla} p^l - 2\mu^l \vec{\nabla} \cdot \left(\bar{\nabla} \langle \vec{v}^l \rangle + \bar{\nabla}^t \langle \vec{v}^l \rangle \right) - g^l \mu^l \mathbb{K}^{-1} \langle \vec{v}^l \rangle + g^l \rho^l \vec{g} \quad (2.40)$$

where we intentionally employed the *superficial velocity*, $\langle \vec{v}^l \rangle = g^l \vec{v}^l$, as the main unknown, together with the liquid pressure p^l . This system, when modelled in 3D, has a total of 4 unknowns (velocity vector and pressure) and 3 equations (X, Y and Z projections for the velocity vector). A fourth equation provided by the mass balance (eq. (2.27)) is therefore added for closure, giving the following system of equations :

$$\begin{cases} \frac{\partial}{\partial t} \left(\rho^l \langle \vec{v}^l \rangle \right) + \frac{1}{g^l} \vec{\nabla} \cdot \left(\rho^l \langle \vec{v}^l \rangle \times \langle \vec{v}^l \rangle \right) = \\ - g^l \vec{\nabla} p^l - 2\mu^l \vec{\nabla} \cdot \left(\bar{\nabla} \langle \vec{v}^l \rangle + \bar{\nabla}^t \langle \vec{v}^l \rangle \right) - g^l \mu^l \mathbb{K}^{-1} \langle \vec{v}^l \rangle + g^l \rho^l \vec{g} \\ \nabla \cdot \langle \vec{v}^l \rangle = 0 \end{cases} \quad (2.41)$$

Last, the Boussinesq approximation allows taking a constant density in the inertial terms of eq. (2.41) while the variations responsible for buoyancy forces can be computed using eq. (1.1a), if the system is incompressible. Hence, the final set of equations is better known as the incompressible *Navier-Stokes* equations, applied to a solidifying melt:

$$\begin{cases} \rho_0^l \left(\frac{\partial \langle \vec{v}^l \rangle}{\partial t} + \frac{1}{g^l} \vec{\nabla} \cdot \left(\langle \vec{v}^l \rangle \times \langle \vec{v}^l \rangle \right) \right) = \\ - g^l \vec{\nabla} p^l - 2\mu^l \vec{\nabla} \cdot \left(\bar{\nabla} \langle \vec{v}^l \rangle + \bar{\nabla}^t \langle \vec{v}^l \rangle \right) - g^l \mu^l \mathbb{K}^{-1} \langle \vec{v}^l \rangle + g^l \rho^l \vec{g} \\ \nabla \cdot \langle \vec{v}^l \rangle = 0 \end{cases} \quad (2.42)$$

Since all conservation equations were presented and simplified by the main assumption of a static solid phase, we may include them in a graphical summary in section 2.1.4

correct definitions of w^l and w^s

Macro models: Rivaux ? Gu beckermann 1999

Micro macro: Tommy Carozzani 2013, guo beckermann 2003, Combeau 2009, Miha Zaloznik 2010 (indirect), P. Thévoz, J.-L. Desbiolles, M. Rappaz, Metallurgical and Materials TransactionsA 20 (2) (1989) 311–322

end by talking about taking air into account and the need for an interface capturing method

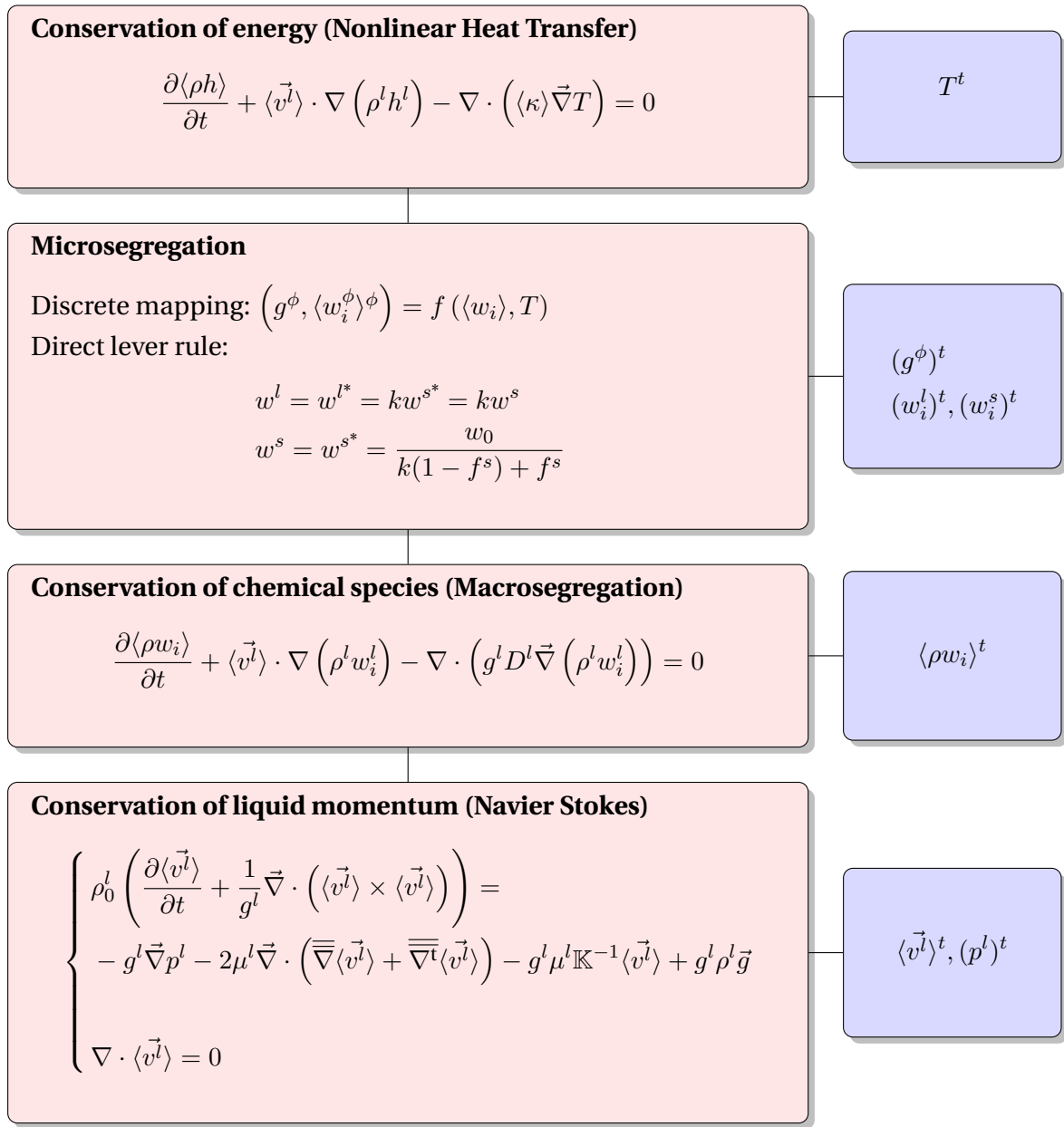


Fig. 2.3 – Graphical resolution algorithm of the conservation equations used in a monodomain macroscopic model to predict macrosegregation. The blue boxes represent the output of each equation at a time step t .

2.2 Eulerian and Lagrangian motion description

2.2.1 Overview

In mechanics, it is possible to describe motion using two well-known motion description: Eulerian and Lagrangian descriptions. To start with the latter, it describes the motion of a particle by attributing a reference frame that moves with the particle. In other words, the particle itself is the center of a reference frame moving at the same speed during time. The position vector, denoted by \vec{x} , is hence updated as follows:

$$\vec{x}^{(t+1)} = \vec{x}^{(t)} + \vec{v}\Delta t \quad (2.43)$$

As such, the total variation of any physical quantity ψ related to the particle can be found by deriving with respect to time, $\frac{d\psi}{dt}$. In contrast to the Lagrangian description, the Eulerian description considers a fixed reference frame and independent of the particle's trajectory. The total variation of ψ cannot be simply described by a temporal derivative, since the particle's velocity is not known to the reference frame, and thus the velocity effect, namely the advective transport of ψ , should also be considered as follows:

$$\frac{d\psi}{dt} = \frac{\partial\psi}{\partial t} + \underbrace{\vec{v} \cdot \nabla \psi}_{\text{Advection Transport}} \quad (2.44)$$

In this case, the LHS term is also known as *total* or *material derivative*. The importance of these motion descriptions is essential to solve mechanics, whether for fluids or solids, using a numerical method like the finite element method (FEM). One of the main steps of this method is to spatially discretise a continuum into a grid of points (nodes, vertices ...), where any physical field shall be accordingly discretized. Now, if we focus on a node where velocity has a non zero value and following the previously made analysis, two outcomes are possible: either the node would be fixed (Eulerian) or it would move by a distance proportional to the prescribed velocity (Lagrangian). In the latter case, points located on the boundaries constantly require an update of the imposed boundary conditions.

From these explanations, one can deduce that an Eulerian framework is suited for fluid mechanics problems where velocities are high and may distort the mesh points, whereas the Lagrangian framework is better suited for solid mechanics problems where deformation velocities are relatively low and should well behave when predicting strains.

Another motion description has emerged some decades ago, [Hirt \[1971\]](#) call it the Arbitrary Langrangian-Eulerian (ALE) method. ALE combines advantages from both previous descriptions as it dictates a Lagrangian behavior at "solid" nodes where solid is deforming, and an Eulerian behavior at "fluid" nodes.

2.2.2 Interface capturing

As no solid deformation is considered in this work, the Eulerian framework is a convenient choice. Although solidification shrinkage is to be considered in the current scope, it will deform the alloy's outer surface in contact with the air. We intend to track this interface and its motion over time via a numerical method. A wide variety of methods accomplish this task while they yield different advantages and disadvantages. Such methods fall into two main classes, either interface tracking or interface capturing, among which we cite: marker-and-cell (MAC) [Harlow et al. 1965], volume of fluid (VOF) [Hirt et al. 1981], phase field methods (PF), level set method (LSM) [Osher et al. 1988], coupled level set - VOF method and others. The interested reader may refer to quick references by Prosperetti [2002] and Maitre [2006] about these methods.

In the past years, the level set method received a considerable attention in many computational fields, specifically in solidification. For this reason, we will focus on this method henceforth, giving a brief literature review and technical details in the next sections.

2.3 Solidification models with level set

In classic solidification problems, the need to track an interface occurs usually at the solid-liquid interface, that is why the phase field method [Karma et al. 1996; Boettinger et al. 2002] and the level set method [Chen et al. 1997; Gibou et al. 2003; Tan et al. 2007] were applied at a microscale to follow mainly the dendritic growth of a single crystal in an undercooled melt. In our case however, when we mention "solidification models using LSM", we do not mean the solid-liquid interface inside the alloy, but it is the alloy(liquid)-air interface that is tracked, assuming that microscale phenomena between the phases within the alloy, are averaged using the previously defined technique in section 2.1.4.

Very few models were found in the literature, combining solidification and level set as stated previously. Du et al. [2001] applied it to track the interface between two molten alloys in a double casting technique. Welding research, on another hand, has been more active adapting the level set methodology to corresponding applications. In CEMEF, two projects use the metal-air level set methodology in welding simulations and showed promising results.

two sentences not more about the contribution of OD and SC

Firstly, Desmaison et al. [2014] ... TODO

Later, Chen [2014] applied it to gas metal arc welding (GMAW) to predict the grain structure in the heat affected zone essentially. More recently, Courtois et al. [2014] used the same methodology but this time to predict keyhole defect formation in spot laser welding. The tracked interface in this case was that between the molten alloy and the corresponding vapor phase.

2.4 The level set method

Firstly introduced by Osher et al. [1988], this method became very popular in studying multiphase flows. It is reminded that the term *multiphase* in computational domains usually refers to multiple fluids, and thus should not be mixed with definition of a phase in the current solidification context. For disambiguation, we shall use *multifluid flow* when needed. The great advantage lies in the way the interface between two fluids, F_1 and F_2 is implicitly captured, unlike other methods where the exact interface position is needed. In a discrete domain, the concept is to assign for each mesh node of position vector \vec{x} , the minimum distance $d_\Gamma(\vec{x})$ separating it from an interface Γ . The distance function, denoted α and defined in eq. (2.45), is then signed positive or negative, based on the fluid or domain to which the node belongs.

$$\alpha(\vec{x}) = \begin{cases} d_\Gamma(\vec{x}) & \text{if } \vec{x} \in F_1 \\ -d_\Gamma(\vec{x}) & \text{if } \vec{x} \in F_2 \\ 0 & \text{if } \vec{x} \in \Gamma_{F1,F2} \end{cases} \quad (2.45)$$

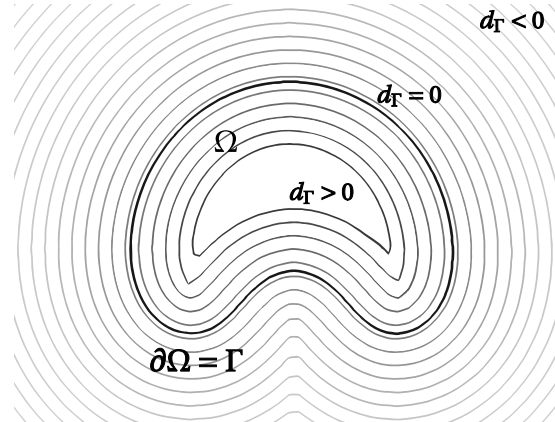


Fig. 2.4 – Schematic of the interface Γ (thick black line) of a rising air bubble (Ω) in water. The other contours represent isovalues of the distance function around and inside the interface contour. Those outside are signed negative whereas inside they are signed positive.

2.4.1 Diffuse interface

The level set has many attractive properties that allows seamless implementation in 2D and 3D models. It is a continuously differentiable C^1 -function. For instance, a *Heaviside* function, denoted H , can be obtained by first order derivation of the level set function. The Heaviside function is continuous but non differentiable, with an

abrupt transition from 0 to 1 across the sharp interface, as follows:

$$H = H(\alpha(\vec{x})) = \begin{cases} 0 & \text{if } \alpha(\vec{x}) < 0 \\ 1 & \text{if } \alpha(\vec{x}) \geq 0 \end{cases} \quad (2.46)$$

With the help of [eq. \(2.46\)](#), we can define the geometric "presence" of a domain with respect to the interface. As such, material properties depend upon this function, which will be discussed later in [section 2.4.2](#). It is established that a steep transition can lead to numerical problems, so the Heaviside function should be smoothed in a fixed thickness. Sinusoidal smoothing in [eq. \(2.47\)](#) is widely used with level set formulations.

$$H = \begin{cases} 0 & \text{if } \alpha(\vec{x}) < -\varepsilon \\ 1 & \text{if } \alpha(\vec{x}) > \varepsilon \\ \frac{1}{2} \left(1 + \frac{\alpha(\vec{x})}{\varepsilon} + \frac{1}{\pi} \sin \left(\frac{\pi \alpha(\vec{x})}{\varepsilon} \right) \right) & \text{if } -\varepsilon \leq \alpha(\vec{x}) \leq \varepsilon \end{cases} \quad (2.47)$$

where the interval $[-\varepsilon; +\varepsilon]$ is an artificial interface thickness around the zero distance. Defining a diffuse interface rather than a sharp one, is also a common approach in phase field methods [[Beckermann et al. 1999](#); [Sun et al. 2004](#)]. It is emphasized that the latter methods give physically meaningful analysis of a diffuse interface and the optimal thickness by thoroughly studying the intricate phenomena happening at the scale of the interface. However, for level set methods, there has not been a formal work leading the same type of analysis. For this reason, many aspects of the level set method lack physical meanings but still computationally useful. In a recent paper by [Gada et al. \[2009\]](#), the authors respond partially to this problem by analysing and deriving conservation equations using a level set in a more meaningful way, but do not discuss the diffuse interface aspect.

The dirac delta function is also an important property to convert surface integrals to volume terms, which could turn useful when modelling surface tension effects for instance, using the *continuum surface force* method (CSF) [[Brackbill et al. 1992](#)]. The dirac function, plotted in [fig. 2.5](#) along with the Heaviside function within an interface thickness of $[-\varepsilon; +\varepsilon]$, is derived from the Heaviside as follows:

$$\delta(\alpha) = \delta(\alpha(\vec{x})) = \frac{\partial H}{\partial \alpha(\vec{x})} = \begin{cases} \frac{1}{2\varepsilon} \left(1 + \cos \left(\frac{\pi \alpha(\vec{x})}{\varepsilon} \right) \right) & \text{if } |\alpha(\vec{x})| \leq \varepsilon \\ 0 & \text{if } |\alpha(\vec{x})| > \varepsilon \end{cases} \quad (2.48)$$

The Heaviside and delta dirac functions can be readily processed to obtain other geometric properties from the level set, which are extremely useful. We mention the most

relevant ones [Peng et al. 1999]:

$$\text{normal vector} : \vec{n} = \frac{\vec{\nabla}\alpha}{\|\vec{\nabla}\alpha\|} \quad (2.49)$$

$$\text{curvature} : \zeta = -\nabla \cdot \vec{n} \quad (2.50)$$

$$\text{surface area of the air-metal interface} : A^\Gamma = \int_{\Omega} \delta(\alpha) \|\vec{\nabla}\alpha\| d\Omega \quad (2.51)$$

$$\text{metal volume} : V^M = \int_{\Omega} H^M d\Omega \quad (2.52)$$

where, for the last two equations, we considered a three-dimensional domain Ω containing two subdomains, metal and air, separated by an interface Γ . It is reminded that for a 2D case, eq. (2.51) evaluates a length instead of the area while eq. (2.52) gives the area instead of volume. Finally, within the diffuse interface, fluids properties may vary linearly or not, depending on the mixing law, which is presented in the next section.

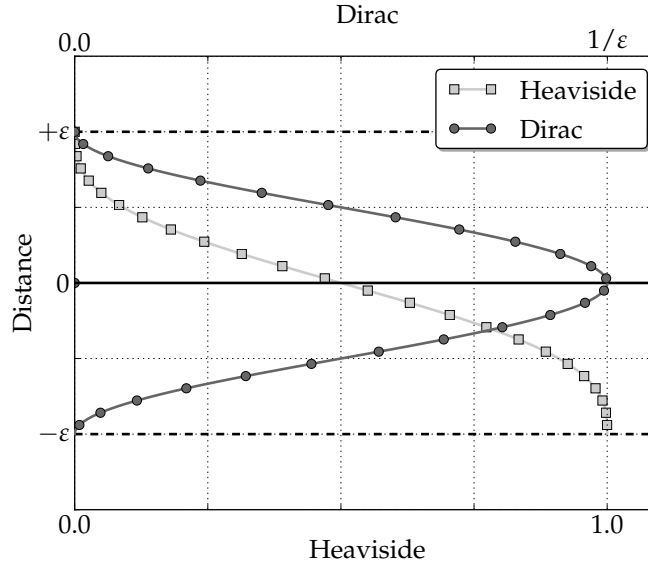


Fig. 2.5 – Schematic of two level properties inside the diffuse interface: Heaviside (lower x-axis) and Dirac delta (upper x-axis) functions. Note that the peak of the dirac function depends on the interface thickness to ensure a unity integral of the delta function over Ω .

2.4.2 Mixing Laws

A *monolithic* resolution style, as opposed to a *partitioned* resolution, is based on solving a single set of equations for both fluids separated by an interface, as if a single fluid were considered. Level set is one many methods that use the monolithic style to derive a single set of conservation equations for both fluids. The switch from one material to the other is implicitly taken care of by using the Heaviside function as well mixing laws. These laws are crucial to define how properties vary across the diffuse

interface in view of a more accurate resolution. The most frequently used mixing law in the literature is the arithmetic law. Other transitions are less known such as the harmonic and logarithmic mixing. The first law is maybe the most intuitive and most used for properties mixture as it emanates from VOF-based methods. If we consider any property ψ , for instance the fluid's dynamic viscosity μ , then the arithmetic law will give a mixed property $\hat{\psi}$ as follows:

$$\hat{\psi} = H^{F_1}\psi^{F_1} + H^{F_2}\psi^{F_2} \quad (2.53)$$

Basically, the result is an average property that follows the same trend as the Heaviside function. As for the harmonic law, it writes:

$$\hat{\psi} = \left(\frac{H^{F_1}}{\psi^{F_1}} + \frac{H^{F_2}}{\psi^{F_2}} \right)^{-1} \quad (2.54)$$

and last, the logarithmic law writes:

$$\hat{\psi} = n^{(H^{F_1} \log_n \psi^{F_1} + H^{F_2} \log_n \psi^{F_2})} \quad (2.55)$$

where n is any real number serving as a logarithm base, which often is either the exponential e or 10. The mixture result with this law is the same, regardless of the value of n . By looking to [fig. 2.6](#), we clearly see that the difference between all three approaches is the property weight given to each side of the level set in the mixture. The arithmetic law, being symmetric, has equal weights, ψ^{F_1} and ψ^{F_2} , in the final mixture. Nevertheless, the asymmetric harmonic mixing varies inside the diffuse interface with a dominant weight of one property over the other. As for the logarithmic mixture, it can be seen as an intermediate transition between the preceding laws. As long

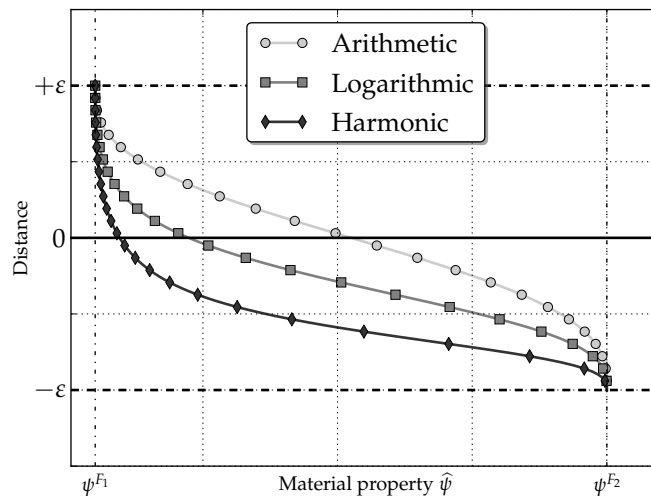


Fig. 2.6 – Three mixing laws, arithmetic, logarithmic and harmonic commonly used in monolithic formulations.

as the interface thickness is small enough, the choice of a mixing law should not drastically change the result, inasmuch as it depends on the discretisation resolution of the interface. This fact made the arithmetic mixing the most applied one, because it is symmetric and easy to implement (no handling of potential division problems like harmonic laws for instance). However, [Stratos et al. \[2008\]](#) claim that the harmonic law proves to conserve better diffusive fluxes at the interface. More recently, an interesting study made by [Ettrich et al. \[2014\]](#) focused on mixing thermal properties using a phase field method. They define a diffuse interface in which they separately mix the thermal conductivity, κ , and the heat capacity, C_v , then compute the thermal diffusivity as the ratio of these properties. Later, the authors compare the temperature field obtained by diffusion to a reference case in order to decide which combination of mixing laws gives the best result. Despite not being directly related to a level set method, this work gives an insight of the mixture possibilities and their effect on a pure thermal diffusion. Otherwise, little work has been found in the literature on the broad effects of mixture types on simulation results in a level set context.

2.5 Interface motion

When a physical interface needs to have topology changes because of fluid structure interaction or surface tension for instance, the level set model can easily follow these changes by a transport step. The idea is the advect the signed distance function, its zero isovalue representing the interface and all other distant isovales, with the velocity field as input. The motion of the interface is thus expressed by:

$$\frac{d\alpha}{dt} = \frac{\partial\alpha}{\partial t} + \vec{v} \cdot \vec{\nabla}\alpha = 0 \quad (2.56)$$

Associated boundary conditions

2.5.1 Level set transport

The finite element method gives the fully discretised weak form of [eq. \(2.56\)](#) by using a convenient set of test functions α^* belonging the hilbertian *Sobolev* space:

$$\int_{\Omega} \alpha^* \frac{\partial\alpha}{\partial t} d\Omega + \int_{\Omega} \alpha^* \vec{v} \cdot \vec{\nabla}\alpha d\Omega = 0 \quad \forall \alpha^* \in \mathcal{H}^1(\Omega) \quad (2.57)$$

The spatial discretisation of α assigns, for each of the total N nodes of a simplex, the following values:

$$\alpha = \sum_N P_j \alpha_j \quad (2.58)$$

Furthermore, with the Galerkin method, we replace test functions by the interpolation functions P_j , then we apply a temporal discretisation for the main unknowns by a forward finite difference in time. Consequently, eq. (2.57) can be recast as follows:

$$\frac{1}{\Delta t} \left(\alpha_j^t - \alpha_j^{t-\Delta t} \right) \int_{\Omega} P_i P_j \, d\Omega + \alpha_j^t \int_{\Omega} \vec{v}^t \cdot \vec{\nabla} P_j \, d\Omega = 0 \quad (2.59a)$$

$$\left[\frac{1}{\Delta t} \int_{\Omega} P_i P_j \, d\Omega + \int_{\Omega} \vec{v}^t \cdot \vec{\nabla} P_j \, d\Omega \right] \alpha_j^t = \frac{1}{\Delta t} \int_{\Omega} \alpha^{t-\Delta t} P_i \, d\Omega \quad (2.59b)$$

$$[\mathcal{M}_{ij} + \mathcal{A}_{ij}] \alpha_j^t = \mathcal{F}_i \quad (2.59c)$$

where \mathcal{M}_{ij} and \mathcal{A}_{ij} are respectively the mass (or capacity) matrix and advection matrix, both written within a local finite element, whereas \mathcal{F}_i is a local vector of known quantities from the previous time step. The solution of the linear system in eq. (2.59c) is the transported distance function.

2.5.2 Level set regularisation

Upon transport the distance function field, a crucial property of the level set may be partially or totally lost over the domain, which is:

$$\begin{cases} \|\vec{\nabla} \alpha\| = 1 \\ \alpha(x, t) = 0 & \text{if } x \in \Gamma(t) \end{cases} \quad (2.60)$$

The closer this L^2 -norm to one, the more regular the level set. An irregular distance function induces cumulative numerical errors in the transport step (eq. (2.56)) and thus results in non conservation of mass, because of spurious distance information. When the transport equation in eq. (2.56) is discretised in time then solved, a *regularisation* (also known as *reinitialisation*) is necessary to conserve as much as possible the property in eq. (2.60).

Figure 2.7 shows the need of regularisation in two different simulations of the same phenomenon: rising air bubble inside water. The importance of this well studied case [Sussman et al. 1994; Hysing et al. 2009] is that the interface between two fluids is highly deformable as the bubble rises because of buoyancy, and therefore the task of tracking the dynamic interface while maintaining an accurate distance function is a considerable numerical task. In the first simulation, the distance contours are squeezed against the zero-distance contour marked by the thick black line. A closer look to the interface reveals undesired distortions, with a "wavy" shape at some points. This effect is evidently an artefact of a level set transport lacking subsequent reinitialisation, inasmuch as the surface tension tends to minimise the total surface area and make it as smooth as possible. Nevertheless, the second simulation unveils much better results, especially how the interface shows no sign of destabilisation. We also note the regular spacing between contours, which is a consequence of conserving the property defined in eq. (2.60). We attribute this improvement to the regularization

done at each time step after the transport. In the forthcoming sections, we present two regularisation methods, then show their strong and weak points.

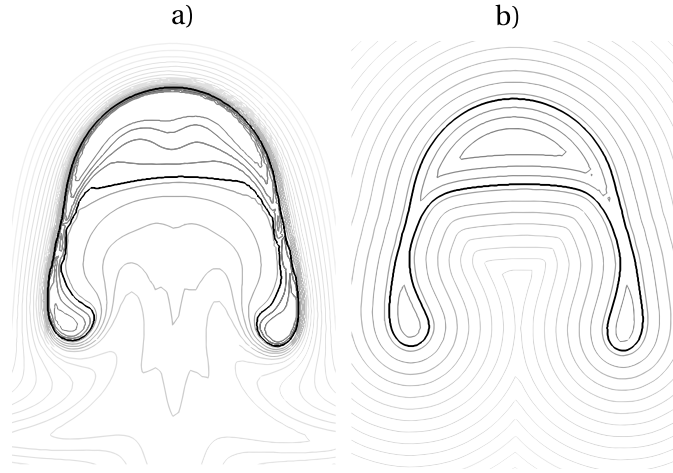


Fig. 2.7 – Schematic of the influence of level set regularisation on the distance function at the same time frame: a) without any regularisation step, the isovalue contours are distorted in the wake of the rising air bubble while being squeezed ahead of it, b) in contrast to regularising the distance function, where the contours maintain their spacing and geometric properties with respect to the tracked interface.

Classic Hamilton-Jacobi reinitialisation

In order to repair a distance function impaired by convective transport, [Sussman et al. \[1994\]](#) proposed solving a classic *Hamilton-Jacobi* equation, given in its most general form:

$$\frac{\partial \alpha}{\partial t} + \mathbb{H}(\alpha, x, t) = 0 \quad x \in \Omega, t > 0 \quad (2.61)$$

where $\alpha(x, t = 0) = \alpha_0$ is the initial value of the distance function. The term \mathbb{H} is known as the *Hamiltonian*. When the sign of the level set and its metric property ($\|\vec{\nabla}\alpha\| = 1$) are considered, [eq. \(2.61\)](#) reduces to:

$$\frac{\partial \alpha}{\partial t} + S(\alpha) \left(\|\vec{\nabla}\alpha\| - 1 \right) = 0 \quad (2.62)$$

where $S(\alpha)$ is a step function giving the sign of the level set as follows:

$$S(\alpha) = \frac{\alpha}{|\alpha|} = \begin{cases} -1 & \text{if } \alpha < 0 \\ 0 & \text{if } \alpha = 0 \\ +1 & \text{if } \alpha > 0 \end{cases} \quad (2.63)$$

The sign function defined in [eq. \(2.63\)](#) is often smoothed to avoid numerical problems, as proposed for instance by [Sussman et al. \[1994\]](#):

$$S(\alpha) = S_\varepsilon(\alpha) = \frac{\alpha}{\sqrt{\alpha^2 + \varepsilon^2}} \quad (2.64)$$

where ε is a smoothing parameter that depends on the mesh size around the interface. However, one should be aware that within the smoothing thickness, the regularised function may suffer from local oscillations because of the reciprocal reinitialisation taking place at each side of the level set. [Peng et al. \[1999\]](#) states that this problem is more likely to happen if the initial level set shows very weak or very steep gradients, and therefore is not regular enough. The authors eventually propose a new sign function which would reinitialise the distance function, as close as possible to the interface without modifying the latter, as follows:

$$S(\alpha) = S_\varepsilon(\alpha) = \frac{\alpha}{\sqrt{\alpha^2 + \|\vec{\nabla}\alpha\|^2\varepsilon^2}} \quad (2.65)$$

Convective reinitialization

A recent work by [Ville et al. \[2011\]](#) introduced another concept for reinitialisation called the *convective reinitialisation*. The idea lies in combining both level set advection and regularisation in a single equation, saving resolution time. The key components of their method starts by defining a pseudo time step, $\Delta\tau$, that is linked to the main time variable through a numerical parameter λ_τ , as follows:

$$\lambda_\tau = \frac{\partial\tau}{\partial t} \quad (2.66)$$

The order of magnitude of λ_τ , which can be seen as a relaxation parameter [see [Vigneaux 2007](#), p. 89], is close to the ratio $h/\Delta t$. Then, the classic Hamilton-Jacobi [eq. \(2.61\)](#) is combined into the convection step by writing:

$$\frac{\partial\alpha}{\partial t} + (\vec{v} + \lambda_\tau \vec{U}) \cdot \vec{\nabla}\alpha = \lambda_\tau S(\alpha) \quad (2.67)$$

where \vec{U} is a velocity vector in the normal direction to the interface, defined by $\vec{U} = S(\alpha)\vec{n}$. the normal vector \vec{n} being previously defined in [eq. \(2.49\)](#). The obvious shortcoming of convective reinitialisation is that it depends on a numerical parameter λ_τ . Another limitation of the method is the use of a sinusoidal filter to modify the distance function by truncating its values beyond a thickness threshold, which is also another parameter to calibrate the resolution. The drawback of truncating the level set is the loss of information far from the interface and the inability to fully reconstruct the distance function. If we denote this threshold by E and the modified level set by $\tilde{\alpha}$ inside

the thickness, then eq. (2.67) is recast as:

$$\frac{\partial \alpha}{\partial t} + (\vec{v} + \lambda_\tau \vec{U}) \cdot \vec{\nabla} \alpha = \lambda_\tau S(\alpha) \sqrt{1 - \left(\frac{\pi}{2E} \tilde{\alpha}\right)^2} \quad (2.68)$$

Equation (2.68) describes the transport and partial reconstruction of the distance function α , knowing its value $\tilde{\alpha}$ inside the thickness E .

Geometric reinitialization

This category of methods go from the level set's basic geometric principle to construct a distance function, instead of solving a partial differential system of equations as in the classic Hamilton-Jacobi reinitialisation. A widely known instance of this category is the *fast marching method* developed by [Sethian \[1996\]](#) and influenced by the [Dijkstra \[1959\]](#)'s method to compute the shortest path in a network of nodes. The method aims to solve the eikonal equation in eq. (2.60) to propagate the distance function in a single direction by *upwinding*, i.e. going from low to high values of the distance function, while preserving a unitary distance gradient.

Direct reinitialisation is another interesting method in the geometric reinitialise category. However, it has not gained noticeable attention in the literature given the terribly cost in terms of computation time and efficiency. The main idea is very simple: reconstruct the distance function over Ω or a subset of Ω , by computing the minimum distance between each mesh node and the interface. It means that, for any point $\vec{x} \in \Omega$, the following constraint should be satisfied [Osher et al. \[2003\]](#):

$$d_\Gamma(\vec{x}) = \min \|\vec{x} - \vec{x}_\Gamma\| \quad \forall \vec{x}_\Gamma \in \partial\Omega = \Gamma, \quad (2.69)$$

A efficient implementation of this method is done by [Shakoor et al. \[2015\]](#) making use of *k-d* trees to limit the search operations of elements and the subsequent distance evaluations in each of these elements. Moreover, the authors give a comparison of the previously stated methods on 2D and 3D cases, showing the great performance of direct reinitialisation when used with k-d trees algorithm, hence we use it in the present work.

To do ?

Interface Remeshing: Importance when using a static level set and more importantly when LS is transported, influence of mixing area *thickness* and *resolution* (i.e. nb of nodes with the area), Isotropic or anisotropic ? the first is more important to composition calculation while the second is more relevant if we mean do thermohydraulics without macrosegregation

Chapter 3

Energy balance with thermodynamic tabulations

Contents

3.1 State of the art	38
3.2 Thermodynamic considerations	38
3.2.1 Volume averaging	38
3.2.2 The temperature-enthalpy relationship	39
3.2.3 Tabulation of properties	40
3.3 Numerical method	43
3.3.1 Enthalpy-based approach	45
3.3.2 Temperature-based approach	45
3.3.3 Convergence	46
3.4 Validation	47
3.4.1 Pure diffusion	47
3.4.2 Convection and diffusion	50
3.5 Application: multicomponent alloy solidification	53
3.5.1 Tabulations	53
3.5.2 Discussion	55

3.1 State of the art

When speaking about macrosegregation, one needs to know that the problem involves phase change. For that, a minimum of four conservation equations are necessary: conservation of mass, momentum, chemical species and energy. The phase change literature contains a wealth of numerical methods to solve energy conservation in solidifying alloys. A comprehensive overview of these methods is given by [Swaminathan. et al. \[1993\]](#). The corresponding equation associates the total average enthalpy to the temperature via intrinsic alloy properties, such as the heat capacity of the phases and the latent heat associated with the phase transformations. However, in the course of solidification and while macrosegregation is taking place, these properties change because the average composition may vary significantly: the transformation paths are thus modified, as well as the phases' composition and heat capacity. Similarly, the latent heat of phase transformations is not a mere constant that could be distributed as a function of the phase fractions assuming only temperature-dependent phases' properties, as often found in the literature [\[Bellet et al. 2009\]](#). It is thus impossible to establish a priori the dependence of the enthalpy with respect to temperature when macrosegregation alters the average composition, even in the case of full thermodynamic equilibrium between phases. In this chapter, we discuss a suitable numerical scheme based on an enthalpy method, already used in the literature to alleviate this macrosegregation-related problem [\[Swaminathan. et al. 1993; Carozzani et al. 2013\]](#). Later on, we introduce a modified formulation, using the effective heat capacity method that increases the original scheme's efficiency.

The method introduced in this chapter is an enthalpy method that makes use of a temperature-based solver. Moreover, it uses tabulated thermodynamic quantities (solidification paths, phases' enthalpy and composition) in a range of average compositions and temperatures as found in the literature [\[Doré et al. 2000; Thuillet et al. 2004; Du et al. 2007\]](#), with the aim of evaluating the total average enthalpy as well as the effective heat capacity. The novelty of the modified method resides in the use of thermodynamic tabulations without losing the advantages of the previous method, thus yielding faster computation times while maintaining a good accuracy.

3.2 Thermodynamic considerations

3.2.1 Volume averaging

The volume averaging technique, presented in [section 2.1.4](#), is the first thing consider when solving the energy equation in the presence of macrosegregation. The reason is that phase quantities that vary with the average composition, have a great impact on the thermal properties, hence on the overall heat transfer in the system. We recall the

basic equation:

$$\langle \psi \rangle = \sum_{\phi} g^{\phi} \langle \psi \rangle^{\phi} \quad (3.1)$$

where g^{ϕ} denotes the volume fraction of phase ϕ in the RVE. It should be emphasized that the averaging technique applies to virtually all thermodynamic variables (enthalpy, density ...). Among these variables, the temperature is also considered to be uniform in the RVE. Applying the volume averaging technique to the energy conservation principle along with interfacial balances between the phases, results in the following averaged equation [Rappaz et al. 2003]:

$$\frac{\partial \langle \rho h \rangle}{\partial t} + \vec{\nabla} \cdot (\langle \rho h \vec{v} \rangle) = \vec{\nabla} \cdot (\langle \kappa \rangle \vec{\nabla} T) + \langle \dot{Q}_V \rangle \quad (3.2)$$

where ρ stands for the density, h the mass enthalpy, \vec{v} the velocity field, κ the thermal conductivity, T the temperature and \dot{Q}_V a possible volume heat source. [Equation \(3.2\)](#) is the standard averaged form of the energy conservation equation used in non-stationary phase change problems.

I could elaborate more in this paragraph by showing the possible equations for the explicit formulation and maybe a figure to show the AlSi7 computation that I did with a very small time step

Once the variational form has been discretized in space and time, two possible resolution schemes emerge: the first is an explicit forward Euler scheme which gives rise to a linear equation where the temperature is known at time t , T^t . This requires very small time steps in the current context, which limits the solver's usability at the scale of industrial applications. The second scheme is the backward Euler or full implicit discretization where terms are function of $T^{t+\Delta t}$. It leads to a nonlinear equation with 2 interdependent unknowns, $\langle \rho h \rangle^{t+\Delta t}$ and $T^{t+\Delta t}$. It is clear that the nature of the temperature-enthalpy relationship plays a central role when formulating the resolution strategy of this nonlinear equation. Generally, it is admitted that, depending on the resolution strategy, it is necessary to express enthalpy as a function of temperature or vice-versa, together with associated partial derivatives, $\frac{d\langle \rho h \rangle}{dT}$ or $\frac{dT}{d\langle \rho h \rangle}$.

3.2.2 The temperature-enthalpy relationship

In solidification problems, additional variables are involved in [eq. \(3.1\)](#) and [eq. \(3.2\)](#), like the transformation path that defines the history of the phase fractions, as well as the average chemical composition $\langle w_i \rangle$, i being the index of the chemical species (only the solutes are considered). The temperature-enthalpy relation averaged over the phases in a given RVE writes:

$$\langle \rho h \rangle = \sum_{\phi} g^{\phi}_{(T, \langle w_i \rangle, \dots)} \rho^{\phi}_{(T, \langle w_i \rangle, \dots)} h^{\phi}_{(T, \langle w_i \rangle, \dots)} \quad (3.3)$$

Chapter 3. Energy balance with thermodynamic tabulations

Note that the volume average enthalpy is approximated by the product $\langle \rho h \rangle^\phi = \langle \rho \rangle^\phi \langle h \rangle^\phi$ in the current work. As stated in the introduction, it becomes clear from [eq. \(3.3\)](#) that phase properties, i.e. average phase density, ρ^ϕ and enthalpy, h^ϕ , are temperature and composition dependent. This equation is the key to convert the average volume enthalpy to temperature (through a procedure named *H2T*) or vice-versa (*T2H*). The values of the different phase fractions g^ϕ (solidification path) and phase enthalpies $\langle \rho h \rangle^\phi$ are thus needed to close the relation.

3.2.3 Tabulation of properties

The complexity of performing a thermodynamic conversion is directly linked to the simplicity of determining the alloy properties, namely the phase fractions and phase enthalpies. In the case of binary alloys and with several assumptions with respect to the system (e.g., linear monovariant temperature composition relationships, constant heat capacity of phases and constant latent heat of transformations, equilibrium approximations between phases) analytical calculations are often used to determine the properties. Nevertheless, analytical relations are more complex or even impossible to derive in the case of multicomponent alloys ($i > 1$). To overcome this problem, one can resort to thermodynamic databases and phase equilibrium calculations to tabulate the transformation paths and the phase enthalpies for a given range of temperatures and average compositions. It is a handy solution for two main reasons: first, the conversion is merely a binary search in a table; secondly, it is a simple solution for coupling with macrosegregation. In this way, phase fractions g^ϕ are tabulated as functions of temperature and average composition, while for each phase ϕ the mass enthalpy, h^ϕ , and the density, ρ^ϕ , are tabulated as functions of temperature and phase intrinsic average compositions $\langle w_i \rangle^\phi$, as well as other possible parameters. [Table 3.1](#) summarizes the steps in order to perform a temperature-to-enthalpy (*T2H*) conversion using the predefined tabulation approach. In step 1, the transformation path is acquired for each average composition and temperature to determine the list of phases, their volume fractions g^ϕ and their intrinsic compositions $\langle w_i \rangle^\phi$. In step 2, the phase enthalpy h^ϕ and density ρ^ϕ are determined by searching for the temperature and the already known phase composition $\langle w_i \rangle^\phi$. In step 3, the average volume enthalpy is computed from the volume fraction, density and mass enthalpy of phases using [eq. \(3.3\)](#). The

Table 3.1 – Tabulation processing for a *T2H* procedure

Step Number	1	2	3
Inputs	$T, \langle w_i \rangle$	$T, \langle w_i \rangle^\phi$	$g^\phi, \rho^\phi h^\phi$
Outputs	$g^\phi, \langle w_i \rangle^\phi$	ρ^ϕ, h^ϕ	$\langle \rho h \rangle$ (eq. (3.3))

methodology to build the tabulations is straightforward. It is based on two main scans. On the one hand, intervals for the variation of the average composition $\langle w_i \rangle$ are chosen from the known alloy composition. These variations have to cover the extreme

3.2. Thermodynamic considerations

values adopted during the simulation, which are not known a priori. An interval is also selected for the variation of temperature. The latter is easier to determine as it usually starts from the initial melt temperature and goes down to the room temperature in a standard casting simulation. For each mapping of composition and temperature, a thermodynamic equilibrium state is computed. The outputs are the number of phases encountered, together with their fraction and intrinsic compositions. The minimum and maximum intrinsic composition for each phase could then be determined. On the other hand, for each phase, a scan of the intrinsic composition and temperature is made to compute the intrinsic properties. The same temperature interval and step as defined earlier are used. Regarding the enthalpy-to-temperature conversion ($H2T$), a backward iterative $T2H$ search is performed. For a known composition $\langle w_i \rangle$, denoting (τ) the iteration index to convert the enthalpy H_{input} , we start with an initial guess for temperature $T^{(\tau=0)}$ then convert it to an enthalpy $H^{(\tau=0)}$ with the $T2H$ conversion. Using an appropriate nonlinear algorithm (Brent is the most versatile in our case), we aim at minimizing the following scalar residual: $R_H = |H_{\text{input}} - H^{(\tau)}|$. Once the algorithm has converged, the temperature $T^{(\tau)}$ is the result of the $H2T$ conversion. It is inferred that the first conversion ($T2H$) is a direct one whereas the latter ($H2T$) is indirect and requires a series of iterative steps; each step being a single $T2H$ resolution. In other words, a $H2T$ conversion is a backward search for a temperature, hence it is slower. This conversion's speed lag is exacerbated when tabulations increase in size (e.g. large number of temperature and composition steps) and complexity (e.g., multi-component industrial alloys used in casting), since the search gets more complicated with the increasing number of input columns (one column for each alloying element).

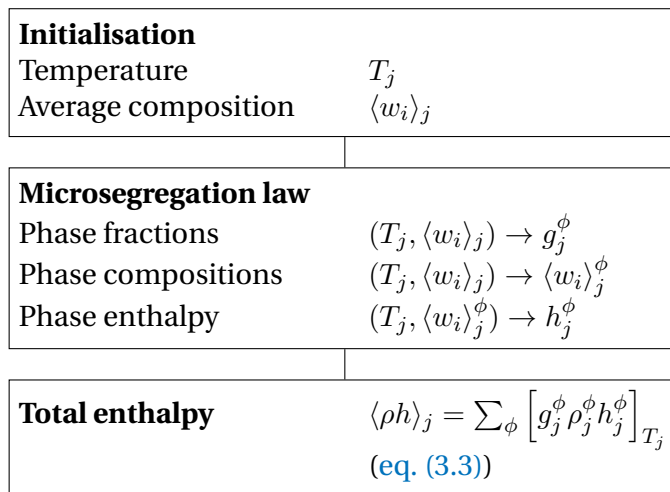


Fig. 3.1 – Algorithm for a single temperature to enthalpy ($T2H$) conversion.

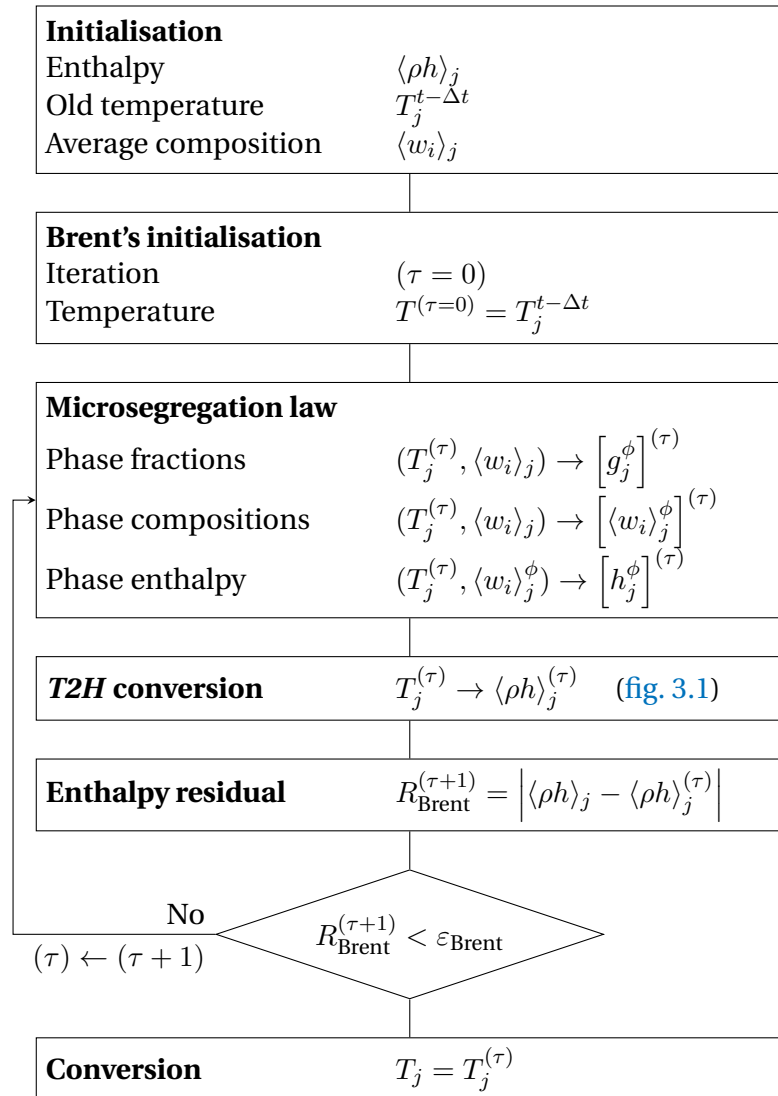


Fig. 3.2 – Algorithm for a single enthalpy to temperature ($H2T$) conversion.

3.3 Numerical method

The finite element method is used to solve the energy conservation as expressed by eq. (3.2). A test function \mathcal{W} belonging to the Hilbertian Sobolev space $\mathcal{H}^1(\Omega_E)$ of continuous integrable test functions is used to formulate the integral variational form of eq. (3.2) [Süli 2000]. A Fourier boundary condition is considered on the domain boundary $\partial\Omega_E$. The domain Ω is discretised using first-order linear simplexes, Ω_E , defined by their number of local nodes (denoted “NbLoc”): triangles in 2D with NbLoc=3 and tetrahedra in 3D with NbLoc=4. The outcome is a residual that we aim to minimize so that the conservation principle is satisfied. Therefore, the weak form writes:

$$\begin{aligned} \forall \mathcal{W} \in M = \{u \in \mathcal{H}^1(\Omega_E)\} \\ \int_{\Omega_E} \mathcal{W} \frac{\partial \langle \rho h \rangle}{\partial t} dV + \int_{\Omega_E} \mathcal{W} \langle \vec{v}^l \rangle \cdot \vec{\nabla} (\rho^l h^l) dV - \int_{\Omega_E} \mathcal{W} \nabla \cdot (\langle \kappa \rangle \vec{\nabla} T) dV - \int_{\Omega_E} \mathcal{W} \langle \dot{Q}_V \rangle dV = 0 \end{aligned} \quad (3.4)$$

where we assumed a static solid phase and an incompressible liquid phase, which allowed recasting the second term of eq. (3.2) into $\langle \vec{v}^l \rangle \cdot \vec{\nabla} (\rho^l h^l)$. The steps for discretizing in time and space the previous equation are well detailed in some book references like Rappaz et al. [2003] and Dantzig et al. [2009]. As for enthalpy and temperature, they are spatially discretised in each simplex using interpolations functions \mathcal{P} , thus defining the nodal values H_j and T_j , respectively:

$$\langle \rho h \rangle = \sum_{j=1}^{\text{NbLoc}} \mathcal{P}_j H_j \quad (3.5)$$

$$T = \sum_{j=1}^{\text{NbLoc}} \mathcal{P}_j T_j \quad (3.6)$$

Note that H_j is a volumetric enthalpy. The Galerkin formulation gives the following expression for the residual contribution at a mesh node i (PS: here i is not the usual solute index) for time step t in a local element Ω_E :

$$\begin{aligned} (R_i^E)^t &= \mathcal{M}_{ij}^E (H_j^t - H_j^{t-\Delta t}) + \mathcal{A}_{ij}^E T_j^t + (\mathcal{K1}_{ij}^E + \mathcal{K2}_{ij}^E) - \mathcal{F}_i^E - \mathcal{S}_i^E = 0 \\ i, j : 1 &\rightarrow \text{NbLoc} \end{aligned} \quad (3.7)$$

Chapter 3. Energy balance with thermodynamic tabulations

where the volumetric contributions are detailed as follows:

$$\text{transient term: } \mathcal{M}_{ij}^E = \int_{\Omega_E} \frac{1}{\Delta t} \mathcal{P}_i \mathcal{P}_j \, dV \quad (3.8)$$

$$\text{advection term: } \mathcal{A}_{ij}^E = \int_{\Omega_E} \rho^l C_p^l \mathcal{P}_i \langle \vec{v}^l \rangle \cdot \vec{\nabla} \mathcal{P}_j \, dV \quad (3.9)$$

$$\text{diffusion term: } \mathcal{K}1_{ij}^E = \int_{\Omega_E} \langle \kappa \rangle \vec{\nabla} \mathcal{P}_i \vec{\nabla} \mathcal{P}_j \, dV \quad (3.10)$$

$$\text{source term: } \mathcal{S}_i^E = \int_{\Omega_E} \mathcal{P}_i \langle \dot{Q}_V \rangle \, dV \quad (3.11)$$

while the surface boundary contributions are given by:

$$\text{boundary condition term 1: } \mathcal{K}2_{ij}^E = \int_{\partial\Omega_E} h_{\text{ext}} \mathcal{P}_i \mathcal{P}_j \, dS \quad (3.12)$$

$$\text{boundary condition term 2: } \mathcal{F}_i^E = \int_{\partial\Omega_E} h_{\text{ext}} T_{\text{ext}} \mathcal{P}_i \, dS \quad (3.14)$$

The surface integrals $\mathcal{K}2_{ij}^E$ and \mathcal{F}_i^E are related to a Fourier-type boundary condition, with h_{ext} as a coefficient of heat exchange and T_{ext} as the external temperature far from the boundary. The energy conservation principle is satisfied when the sum of the residual contributions coming from all the mesh elements is zero. In other words, the following global residual defined by the assembly of these contributions, should be minimized:

$$(R_i)^t = \mathcal{M}_{ij} \left(H_j^t - H_j^{t-\Delta t} \right) + \mathcal{A}_{ij} T_j^t + (\mathcal{K}1_{ij} + \mathcal{K}2_{ij}) T_j^t - \mathcal{F}_i - \mathcal{S}_i = 0 \quad (3.15)$$

$i, j : 1 \rightarrow \text{NbGlob}$

where the global tensors \mathcal{M}_{ij} , \mathcal{A}_{ij} , $\mathcal{K}1_{ij}$, $\mathcal{K}2_{ij}$, \mathcal{F}_i and \mathcal{S}_i contain respectively, after an assembly step, the contributions of the local matrices \mathcal{M}_{ij}^E , \mathcal{A}_{ij}^E , $\mathcal{K}1_{ij}^E$, $\mathcal{K}2_{ij}^E$, \mathcal{F}_i^E and \mathcal{S}_i^E from each discretised element in the domain Ω . Accordingly, the indices i and j refer to global node numbers, where the total number of nodes is denoted by "NbGlob". It is clear that the global residual inherits the dependence between enthalpy and temperature. This is shown in eq. (3.15) where the average volume enthalpy is a function of the temperature. It infers that this residual is a non-linear function; therefore minimizing it requires an iterative non-linear algorithm. Our choice settles on the Newton-Raphson method, known for its quadratic convergence speed. A solidification problem can induce severe non-linearities from the release of the latent heat (which itself is temperature-composition dependent) and the variations of the thermophysical properties of the alloy with respect to temperature and average composition. This algorithm could thus treat such variations. Considering the link between enthalpy and temperature, eq. (3.15) may be solved either for enthalpy or for

temperature as a nodal unknown; hence both formulations are presented hereafter.

3.3.1 Enthalpy-based approach

The residual is re-written using a Taylor series expansion to the first order for a non-linear iteration (ν) :

$$(R_i)^{(\nu+1)} = (R_i)^{(\nu)} + \left(\frac{dR}{dH} \right)_{ij}^{(\nu)} \Delta H_j^{(\nu)} + \mathcal{O}(H_j^2) \quad (3.16)$$

Neglecting the second order terms, the suggested correction at each iteration in view of cancelling the residual and giving the new value $H_j^{(\nu)}$, is given by the linear system in [eq. \(3.17\)](#) relative to what we call a *Hsolver*:

$$\left(\frac{dR}{dH} \right)_{ij}^{(\nu)} (H_j^{(\nu+1)} - H_j^{(\nu)}) = -R_i^{(\nu)} \quad (3.17)$$

where $\frac{dR}{dH}$ is a global tangent matrix yielding the variations of the residual with respect to the enthalpy in the last iteration, $H_j^{(\nu)}$. If [eq. \(3.7\)](#) is considered, then the contribution of an element Ω_E writes:

$$\left(\frac{dR}{dH} \right)_{ij}^{(\nu)E} = \underbrace{\mathcal{M}_{ij}^E + \mathcal{A}_{ij}^E \left(\frac{dT}{dH} \right)_j^{(\nu)}}_{\text{no sum on } j} + \underbrace{(\mathcal{K}1_{ij}^E + \mathcal{K}2_{ij}^E) \left(\frac{dT}{dH} \right)_j^{(\nu)}}_{\text{no sum on } j} \quad (3.18)$$

[Equation \(3.18\)](#) is the core of the enthalpy-based solver. The resolution of [eq. \(3.17\)](#) then yields a new estimate of the vector of nodal enthalpies $H^{(\nu+1)}$, which are the only unknowns to be solved for. Once determined at iteration (ν), convergence tests are performed (refer to section

3.3.2 Temperature-based approach

Similarly to the *Hsolver*, the local residual is recast for a nonlinear iteration (ν), leading this time to an iterative temperature correction:

$$\left(\frac{dR}{dT} \right)_{ij}^{(\nu)} (T_j^{(\nu+1)} - T_j^{(\nu)}) = -R_i^{(\nu)} \quad (3.19)$$

where $\frac{dR}{dT}$ is a global tangent matrix yielding the variations of the residual with respect to temperature $T_j^{(\nu)}$ at the previous iteration. This solver will be referred to as *Tsolver*.

The contribution of an element Ω_E to this tangent matrix is evaluated as:

$$\left[\left(\frac{dR}{dT} \right)_{ij}^{(\nu)} \right]^E = \underbrace{\mathcal{M}_{ij}^E \left(\frac{dH}{dT} \right)_j^{(\nu)}}_{\text{no sum on } j} + \mathcal{A}_{ij}^E + (\mathcal{K}1_{ij}^E + \mathcal{K}2_{ij}^E) \quad (3.20)$$

In contrast to the previous solver, eq. (3.20) is the core of the temperature-based solver. The resolution of eq. (3.19) then yields a new estimate of the vector of nodal temperatures $T^{(\nu+1)}$, which are the only unknowns to be solved for. Once updated for iteration (ν) , convergence tests are performed (refer to section

3.3.3 Convergence

The previous two sections described the iterative resolution of the same discretised energy conservation by both Tsolver and Hsolver. However, in eqs. (3.18) and (3.20), an important term emerges from the tangent matrix evaluation describing the variations between temperature and enthalpy: $\frac{dH}{dT}$ (or $\frac{dT}{dH}$). This term invokes the previously mentioned temperature-enthalpy tabulations which depend on the alloy composition. Consequently, $\frac{dH}{dT}$ (or $\frac{dT}{dH}$) has a great influence on the convergence of the Tsolver (respectively the Hsolver). When eq. (3.17) or eq. (3.19) is solved at iteration (ν) , this term is written using a finite difference:

$$\textbf{Tsolver} \quad \left(\frac{dH}{dT} \right)_j^{(\nu+1)} = \frac{\langle \rho h \rangle_j^{(\nu+1)} - \langle \rho h \rangle_j^{(\nu)}}{T_j^{(\nu+1)} - T_j^{(\nu)}} \quad (3.21)$$

$$\textbf{Hsolver} \quad \left(\frac{dT}{dH} \right)_j^{(\nu+1)} = \frac{T_j^{(\nu+1)} - T_j^{(\nu)}}{\langle \rho h \rangle_j^{(\nu+1)} - \langle \rho h \rangle_j^{(\nu)}} \quad (3.22)$$

For the Tsolver, the enthalpy $\langle \rho h \rangle_j^{(\nu)}$ is needed to evaluate eq. (3.21). In contrast, the Hsolver requires the value of $T_j^{(\nu)}$ to evaluate the corresponding eq. (3.22). In both cases, the unknown is determined by the temperature-enthalpy relation. The indices next to the mentioned unknowns indicate that this relation is used for each iteration (ν) at each mesh node j , hence affecting the global resolution time between the two solvers. The Hsolver needs a $H2T$ to evaluate $\frac{dT}{dH}$, whereas the Tsolver needs a $T2H$ to evaluate $\frac{dH}{dT}$. The flowchart in ?? demonstrates the process. It can be seen that Tsolver uses solely $T2H$ procedure and the thermodynamic tabulations to determine the enthalpy, hence the term $\frac{dH}{dT}$. On the other hand, Hsolver repeats the same procedure a finite number of times in order to determine a temperature output through $H2T$ and use it to compute $\frac{dT}{dH}$. This algorithmic difference leverages the Tsolver in terms of computation time providing the same numerical accuracy while conserving the total system energy.

Convergence tests are necessary at the end of each iteration of the energy solver to

determine the convergence status of the algorithm. In the context of the Tsolver for instance, the residual is re-evaluated with the newly determined temperature $T_j^{(\nu+1)}$ and enthalpy $H_j^{(\nu+1)}$ so eq. (3.15) rewrites:

$$(R_i)^{(\nu+1)} = \mathcal{M}_{ij} \left(H_j^{(\nu+1)} - H_j^{t-\Delta t} \right) + \mathcal{A}_{ij} T_j^{(\nu+1)} + (\mathcal{K}1_{ij} + \mathcal{K}2_{ij}) T_j^{(\nu+1)} - \mathcal{F}_i - \mathcal{S}_i$$

$$i, j : 1 \rightarrow \text{NbGlob}$$
(3.23)

The norm of the current residual, $\|R^{(\nu+1)}\|$, is compared to a fixed small value $\varepsilon_R \approx [10^{-5}; 10^{-4}]$. The resulting temperature variation, $|T_j^{(\nu)} - T_j^{(\nu-1)}|$, should also respond to similar criterion between two consecutive iterations. For that purpose, we compare it to another fixed value $\varepsilon_T \approx [10^{-3}; 10^{-2}]$. Convergence is ultimately achieved when the following criteria are simultaneously met:

$$\begin{cases} \|R^{(\nu+1)}\| < \varepsilon_R \\ \text{Max}_{j:1 \rightarrow \text{NbGlob}} |T_j^{(\nu+1)} - T_j^{(\nu)}| < \varepsilon_T \end{cases}$$
(3.24)

A comparison of both solver formulations is done in the hereafter test cases section.

3.4 Validation

3.4.1 Pure diffusion

The two solvers are first tested in a purely diffusive case for a one-dimensional solidification configuration. Predictions with a 1D front tracking model [Gandin 2000] is used as a benchmark. It provides solutions for the temperature and solid fraction during directional solidification of a 10 cm long Al-7 wt.% Si ingot. The melt, with initial uniform temperature, is cooled with a heat exchange coefficient (assuming a Fourier boundary condition) from one side, the other side being adiabatic. All values for alloy properties, initial and boundary conditions and numerical parameters are listed in table 3.2. For this simple test case, we use linear temperature dependence of the intrinsic phase enthalpies, that is $\langle \rho h \rangle^s = \langle \rho C_p \rangle T$ and $\langle \rho h \rangle^l = \langle \rho C_p \rangle T + \rho L$, where $\langle \rho C_p \rangle$ is the heat capacity per unit volume and ρL is the latent heat per unit volume. Values for $\langle \rho C_p \rangle$ and ρL , as well as for the thermal conductivities, $\kappa = \langle \kappa^l \rangle = \langle \kappa^s \rangle$, are taken constant. Moreover, a Gulliver Scheil approximation is used to compute a single temperature – fraction of solid relationship in the absence of macrosegregation. This is done assuming a linear binary phase diagram and thus requires using the properties listed in table 3.2, i.e. the segregation coefficient, k , the liquidus slope, m_L , the liquidus temperature, T_L , and the eutectic temperature, T_E . Figure 3.5 show the comparison with the Hsolver and Tsolver. The cooling curves and liquid fraction results are found superimposed to the front tracking solution, thus giving validation

Chapter 3. Energy balance with thermodynamic tabulations

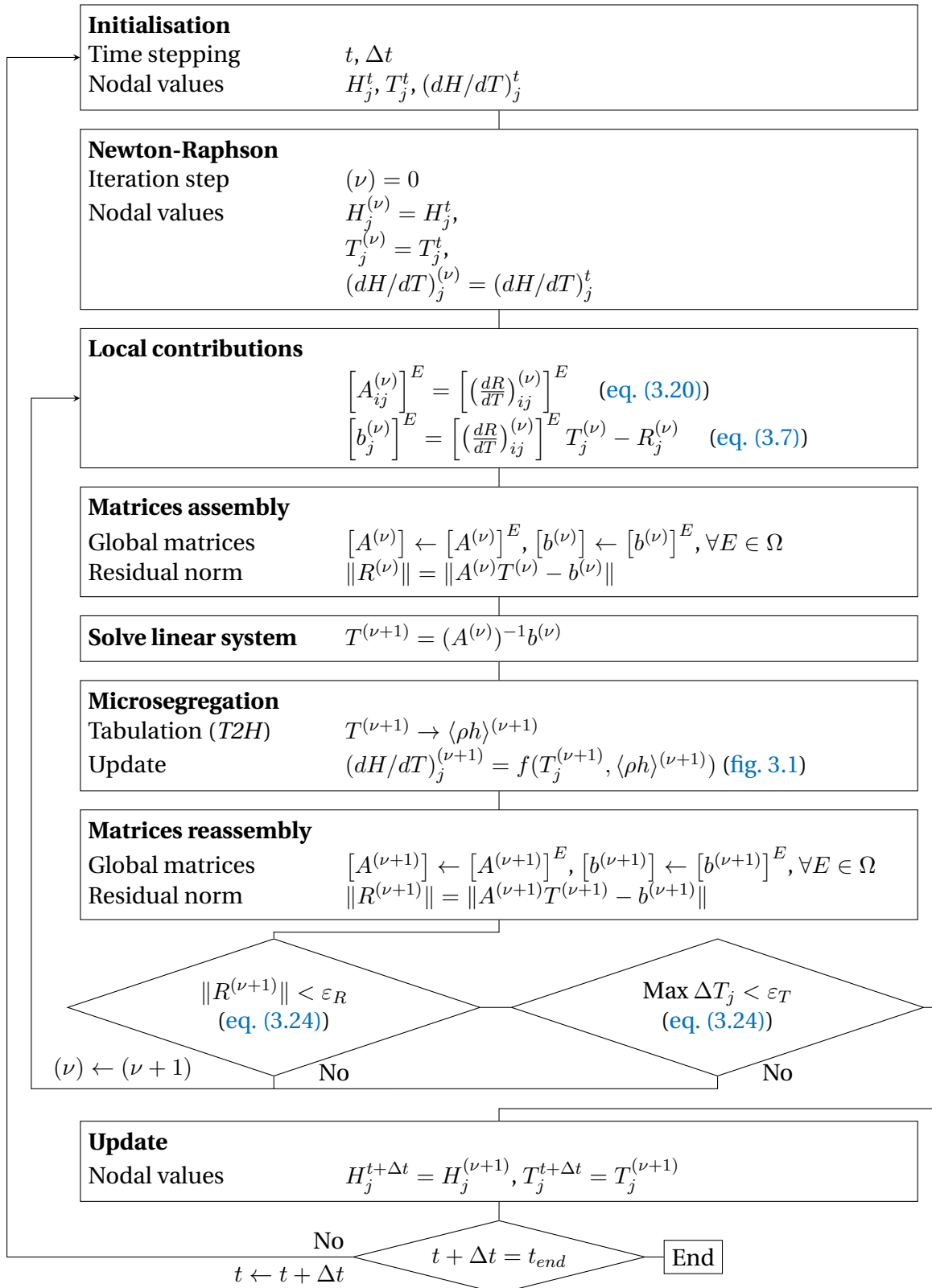


Fig. 3.3 – Resolution algorithm of the temperature-based solver.

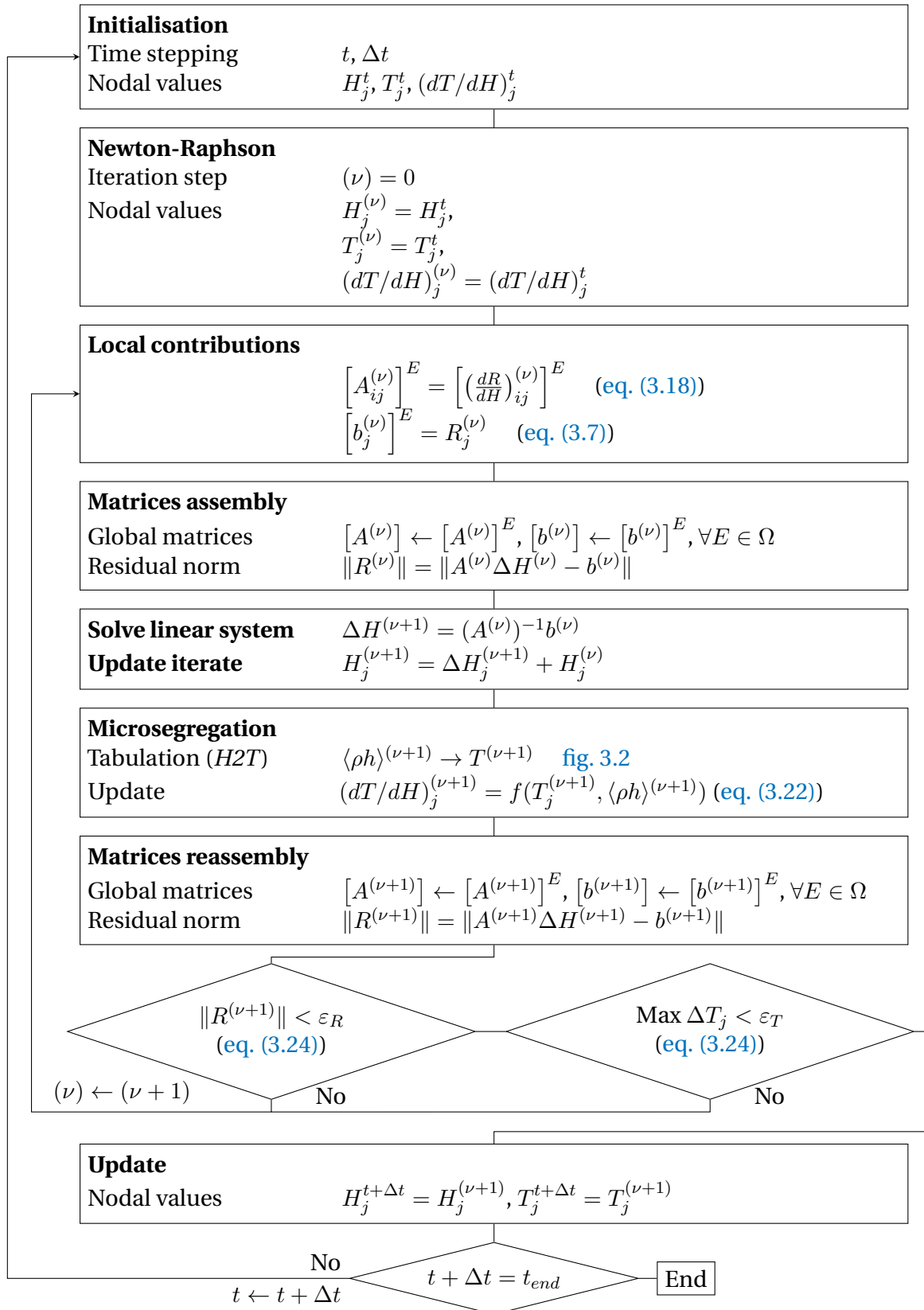


Fig. 3.4 – Resolution algorithm of the enthalpy-based solver.

Chapter 3. Energy balance with thermodynamic tabulations

of the implementation as well as the iterative schemes presented above to solve the energy conservation

Table 3.2 – Parameters for the pure diffusion test case with an Al-7 wt.% Si alloy presented in fig. 3.5

Parameter	Symbol	Value	Unit
Nominal composition	$\langle w \rangle_0$	7	wt.%
Liquidus temperature	T_L	618	°C
Eutectic temperature	T_E	577	°C
Segregation coefficient	k	0.13	–
Liquidus slope	m_L	-6.5	K wt.% ⁻¹
Heat capacity (liquid and solid)	ρC_p	2.6×10^6	J m ⁻³ K ⁻¹
Enthalpy of fusion	ρL	9.5×10^8	J m ⁻³
Thermal conductivity (liquid and solid)	κ	70	W m ⁻¹ K ⁻¹
Heat transfer coefficient	h_{ext}	500	W m ⁻² K ⁻¹
External temperature	T_{ext}	100	°C
Initial temperature	T_0	800	°C
Ingot length		0.1	m
FE mesh size		10^{-3}	m
Time step	Δt	0.1	s
Convergence criterion (residual)	ε_R	10^{-6}	–
Convergence criterion (temperature)	ε_T	10^{-2}	K

3.4.2 Convection and diffusion

Conservation equations in **Table 2** are for mass, momentum and chemical species. As for energy, they are presented after the volume averaging technique has been applied [Ni et al. 1991; Dantzig et al. 2009]. Moreover, an assumption of a static and non deformable solid phase is made. Consequently, the mechanical model is reduced to the conservation of momentum in the liquid phase. This assumption also yields some other consequences on the mass balance and the liquid momentum conservation. In the latter, a Darcy term is added to take into account the dissipative interfacial stress in the porous-like mushy zone. Its main parameter is the permeability of the mushy zone, K . It is considered isotropic, hence reducing to a scalar which is given by the Carman-Kozeny relation, based on the secondary dendrite arm spacing λ_2 : $K = \frac{g^{l^3} \lambda_2^2}{180(1-g^l)^2}$. The liquid density being taken constant, its spatial variations as a function of temperature and average composition are still needed to compute thermosolutal convection forces. For that purpose, the Boussinesq approximation

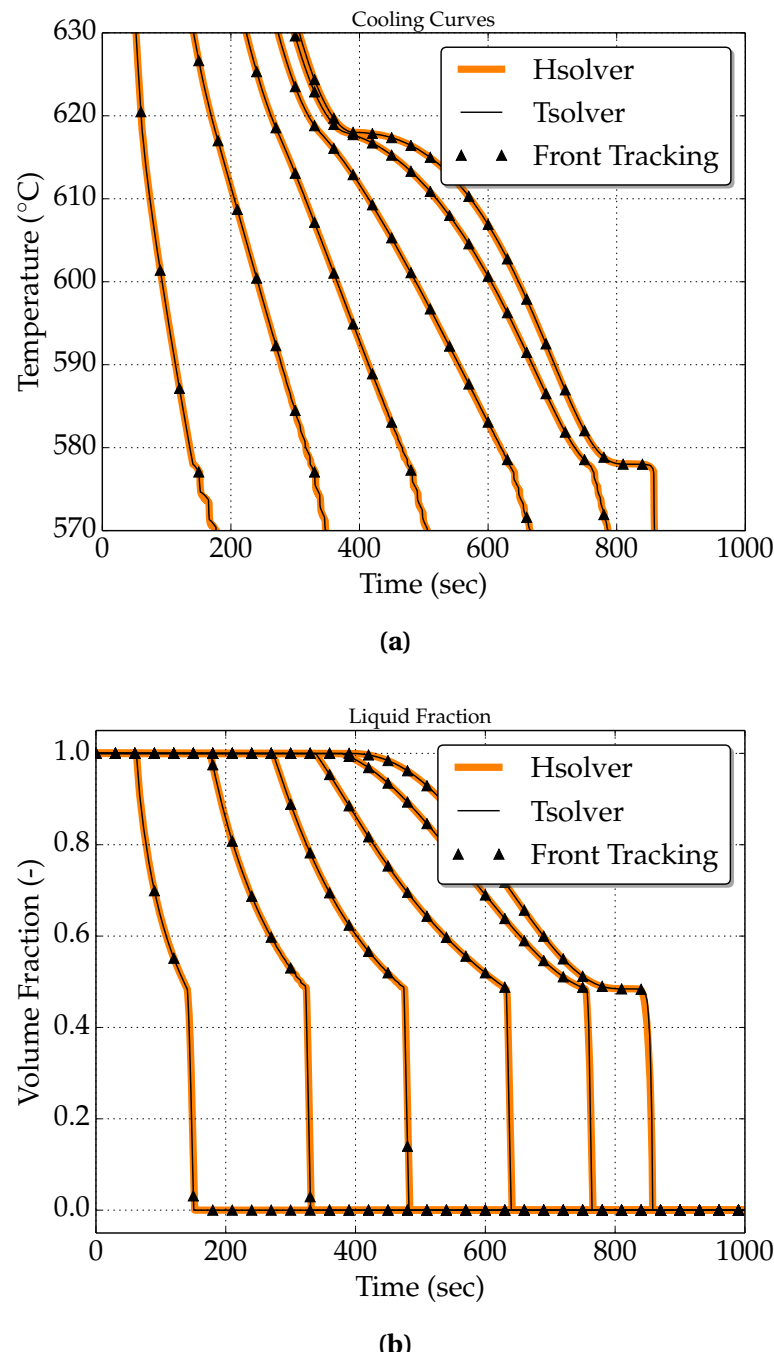


Fig. 3.5 – Computed unidirectional heat diffusion during solidification of an Al-7 wt.% Si alloy using (orange) the enthalpy method and (black) the temperature method, comparison being made for (a) cooling curves and (b) the liquid fraction history. Each curve corresponds to a position along the sample, from 0 cm (cooling side) to 10 cm (insulated side), with 2 cm spacing between the positions.

$\langle \rho \rangle^l = \rho_{\text{ref}} \left(1 - \beta_T (T - T_0) - \beta_{\langle w \rangle^l} (\langle w \rangle^l - w_0^l) \right)$ is used, considering the thermal β_T and solutal $\beta_{\langle w \rangle^l}$) expansion coefficients and a reference density, ρ_{ref} , defined at a reference temperature T_0 and reference composition w_0^l . Values for the references are taken at the liquidus temperature and the nominal composition of the alloy, $\langle w \rangle_0$ [Carozzani et al. 2013]. More details about the FE formulation can be found in the Ph.D work of Rivaux [2011] and Carozzani [2012]. The Tsolver's ability to be coupled with

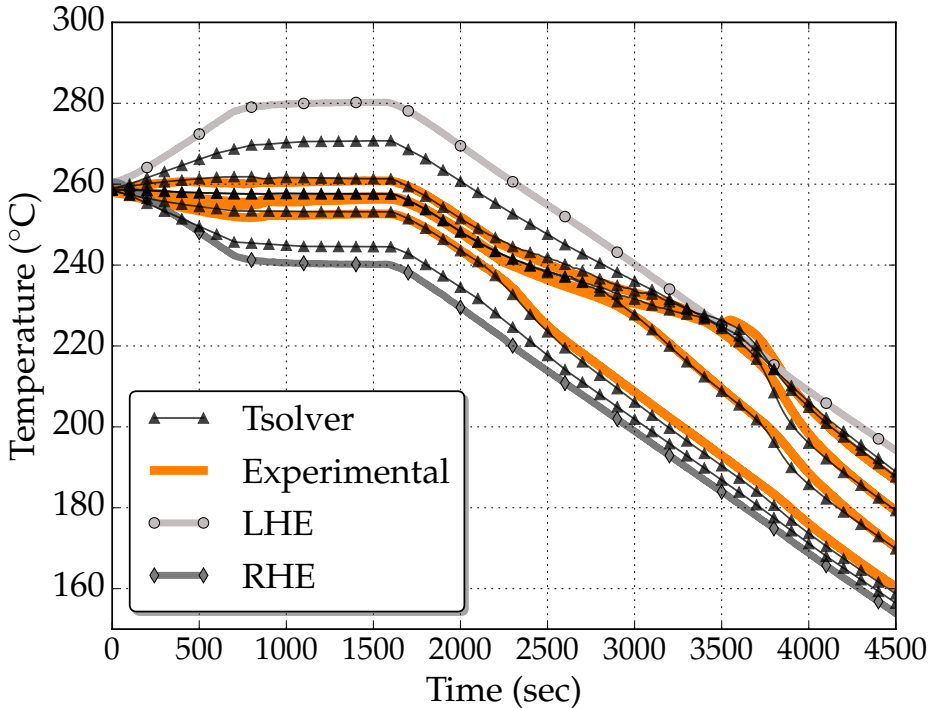


Fig. 3.6 – Experimental cooling curves overlap with the results of the 3D FE convection-diffusion simulation. The left (LHE) and right (RHE) heat exchangers impose the boundary temperature in the experiment.

various physical phenomena like macrosegregation and fluid flow in porous medium is displayed in this test case. Details about fluid flow resolution will not be given in this section, but rather in the next chapter. It consists of a solidification benchmark where a 10 cm width \times 6 cm height \times 1 cm thick cavity containing a Sn-3 wt.% Pb melt is cooled down from its two narrowest vertical sides using heat exchangers (LHE: left heat exchanger, RHE: right heat exchanger). The experiment, inspired by Hebditch et al. [1974] similar set up, has been revisited by Hachani et al. [2012] who performed the solidification with better controlled conditions and using an increased number of samples for composition analysis. Recently, a successful attempt to simulate the experiment was carried out by Carozzani et al. [2013] relying on an enthalpy resolution. All details regarding geometry, finite element discretization, material properties and boundary conditions can be found in the latter reference. For this computation, solidification paths, phase compositions and phase enthalpies were determined by a

thermodynamic module dedicated to equilibrium calculations for binary alloys. The 3D simulation results in [fig. 3.6](#) show a satisfactory agreement with the experimental temperature measurements recorded at mid heights of the cavity and uniformly distributed along its width [[Carozzani et al. 2013](#)]. In fact, simulation results with the Tsolver and the Hsolver were found to be almost superimposed, as shows [fig. 3.6](#). Regarding the computation, the Tsolver resolution proves to be faster than the Hsolver used by [Carozzani et al. \[2013\]](#): a process time of 7000s required a computation time of 90 hours 13 minutes compared to 114 hours 21 minutes spent by the enthalpy resolution with 32 cores on the same cluster. The gain factor is about 20%.

3.5 Application: multicomponent alloy solidification

We have shown that the efficiency of the temperature-based resolution resides in its performance when combined with thermodynamic tabulations. A multicomponent alloy consists of at least two solute elements, and therefore the tabulation size increases, hence the number of search operations also increases. To demonstrate the speed-up ability of the temperature-based approach while predicting all phase transformations during macrosegregation caused solely by mass diffusion, we consider the solidification of a ternary alloy, Fe-2 wt.% C-30 wt.% Cr. In order to neglect fluid flow resolution, we assume that solidification in this case is so slow that no forces are generated inside the melt, while additionally all buoyancy forces are also neglected, so no momentum conservation is solved in this section. As illustrated in [fig. 3.7a](#), the alloy domain has a cylinder shape close to 3-inch height \times 1-inch diameter. Exact values are reported in [table 3.3](#) with all material properties, initial and boundary conditions, as well as numerical parameters for the simulations. The melt steel is initially at 1395 °C. The temperature of the bottom surface is imposed with a constant decreasing rate of 0.1 K s^{-1} starting with 1380 °C, i.e. 40 °C higher than the nominal liquidus temperature, as shown in [fig. 3.7b](#). The other surfaces are kept adiabatic. The cylinder is held in a vertical position. [Figure 5c](#) also provides the transformation path of the alloy at nominal composition, i.e. assuming no macrosegregation and full thermodynamic equilibrium as computed with ThermoCalc and the TCFE6 database [[TCFE6 2010; Andersson et al. 2002](#)]. A total of 5 phases need to be handled, the characteristic temperature for their formation being reported in [fig. 3.7b](#).

Figure 5c: Computed transformation path [[TCFE6 2010; Andersson et al. 2002](#)] at nominal composition for the alloy Fe-2 wt.% C-30 wt.% Cr.

3.5.1 Tabulations

update from last corrected version of the article

Full thermodynamic equilibrium is considered in the present case. Due to macrosegregation, the average composition is expected to continuously vary in time and space

Chapter 3. Energy balance with thermodynamic tabulations

during casting. Transformation paths are thus determined a priori for a set of average compositions around the nominal value. Hence, carbon content is arbitrarily varied in the interval [1.8 wt.%, 2.2 wt.%] while chromium content variation is in the interval [27 wt.%, 33 wt.%]. The offset of $\pm 10\%$ with respect to the nominal composition value allows tabulating relatively small composition steps to ensure a fairly accurate mapping when compared to the corresponding ternary phase diagram. The average composition step is 0.04 wt.% for carbon and 0.6 wt.% for chromium, thus representing 2% intervals with respect to the nominal composition. The temperature varies in the interval [100 °C, 1600 °C] by 5 °C steps. For each triplet (carbon content in wt.% C, HERE, chromium content in wt.% Cr, HERE, temperature in K) corresponds a phase fraction g^ϕ and a pair of intrinsic phase composition (HERE). For the 5 phases listed in **Figure 5c** (LIQ≡liquid, BCC≡ferrite, FCC≡austenite, M₇C₃ ≡carbide, CEM≡cementite), the enthalpy h^ϕ and density ρ^ϕ , are tabulated as functions of temperature and phase intrinsic composition. If this latter input lies between two tabulated values, a linear interpolation is performed to determine the output, i.e. phase enthalpy and density. With the advancement of solidification, the liquid is enriched with solute by macrosegregation, which enables new solidification paths. It means that the primary solidifying phase is not necessarily the same as when considering the nominal composition. For this reason, the tabulation approach is interesting inasmuch as it provides phase transformation paths and values of phase properties that are compatible with the system's actual composition. **Figure 6** summarizes the tabulated thermodynamic data for two sets of average composition for the considered ternary system. Note that in the present test case, phase densities are taken constant ($\rho^s = \rho^l = 6725 \text{ kg m}^{-3}$). Therefore they are not tabulated. With this assumption, no shrinkage occurs upon phase change.

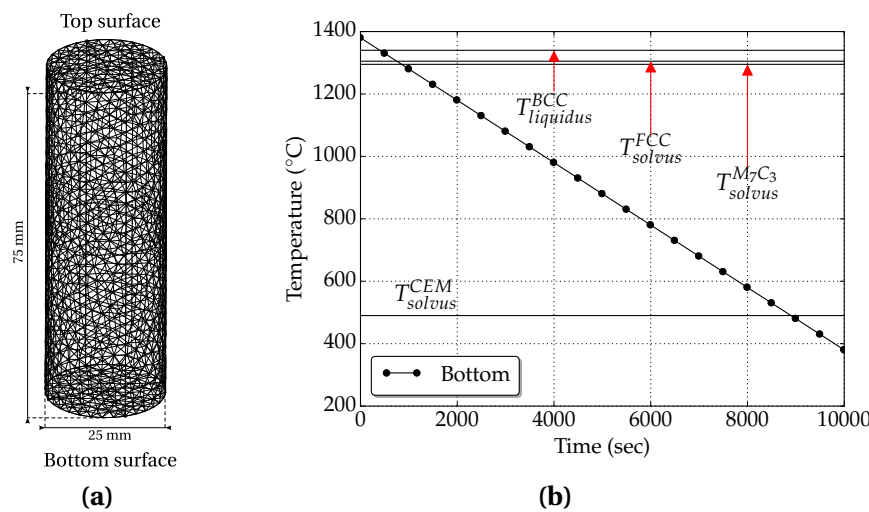


Fig. 3.7 – Configurations for directional casting of (a) a 1 inch diameter × 3 inches height cylindrical domain for which (b) temperature-time conditions are imposed at its bottom surface.

3.5.2 Discussion

A first case is considered without macrosegregation, that is, all mechanical driving forces are bypassed, leading to a static melt. This is achieved by nullifying the thermal and solutal expansion coefficients, which is equivalent to a constant density in space and time, i.e. no Boussinesq force is considered. This way, the average composition may only vary due to diffusion in the liquid phase according to Eq. 20 where the convection term is neglected. Diffusion is significantly small in the present case and can be neglected too. In such a case, the composition distribution maintains a homogeneous aspect throughout the sample during the entire cooling sequence. The phase transformations then are necessarily expected to follow the unique path shown in **Figure 5c**. After 407 s of cooling, the liquidus isotherm enters the bottom surface of the geometry and starts its upward propagation, marking the solidification onset. Figure 7 presents the simulation results at 3 successive times for the distribution of the solute species and the temperature, as well as for the fraction of phases listed in **Figure 5c**. At 600 s, a fully liquid region is still largely present while the mushy zone is made of liquid plus the primary solid phase (ferrite). At 10560 s, the sample is full solid, with fractions of ferrite and cementite that corresponds to the values read in **Figure 5c** at low temperature. At the selected intermediate time, the presence of 4 phases is found. The solid region at the bottom of the cylinder is made of ferrite, austenite plus carbide, the temperature being still too high to permit the cementite to form. The mushy zone above the solid region is characterized by the presence of 3 phases due to a peritectic reaction taking place that progressively transform ferrite into austenite in the presence of liquid. It can be noticed that the phase fraction isovalues in Figure 7 (at 600 s) are horizontal, owing this to two factors: the first is the temperature field, which varies unidirectionally from bottom to top, controlled by thermal diffusion, while the second is the uniform average composition throughout the sample due to the absence of convection. In fact both factors are consequences of the flow absence, which would transport heat and solute by advection, thus inevitably changing the phase distribution. The succeeding phase change is a solid-state transformation where α -ferrite and the carbide M7C3 react to form cementite at 490 °C at nominal composition, as shown in [fig. 3.7b](#). The reaction is relatively slow, ending with 28% of cementite and 72% of α -ferrite.

Chapter 3. Energy balance with thermodynamic tabulations

Table 3.3 – Solidification parameters for the Fe-2 wt.% C-30 wt.% Cr alloy.

Parameter	Symbol	Value	Unit
Nominal composition	$\langle w_C \rangle_0$	2	wt.%
	$\langle w_{Cr} \rangle_0$	30	wt.%
Characteristic temperatures	T_{bottom}	fig. 3.7b	°C
Phase fraction	g^ϕ	Tabulations	REF –
Phase enthalpy	$\langle h \rangle^\phi$	Tabulations	–
Phase composition	$\langle w_C \rangle^\phi$	Tabulations	wt.%
Phase composition	$\langle w_{Cr} \rangle^\phi$	Tabulations	wt.%
Diffusion coefficients	$\langle D_C \rangle^l$	15×10^{-10}	$\text{m}^2 \text{s}^{-1}$
	$\langle D_{Cr} \rangle^l$	15×10^{-10}	$\text{m}^2 \text{s}^{-1}$
Dynamic viscosity	μ^l	2×10^{-3}	Pa s
Thermal expansion coefficient	β_T	8.96×10^{-5}	K^{-1}
Solutal expansion coefficient	$\beta_{\langle w_C \rangle^l}$	1.54×10^{-3}	wt.\%^{-1}
	$\beta_{\langle w_{Cr} \rangle^l}$	1.72×10^{-2}	wt.\%^{-1}
Thermal conductivity in the solid	$\langle \kappa^s \rangle$	40	$\text{W m}^{-1} \text{K}^{-1}$
Thermal conductivity in the liquid	$\langle \kappa^l \rangle$	28	$\text{W m}^{-1} \text{K}^{-1}$
Dendrite arm spacing	λ	60×10^{-6}	m
Density	ρ_{ref}	6725	kg m^{-3}
Reference composition (carbon)	$\langle w_C \rangle_{\text{ref}}^l$	2	wt.%
Reference composition (chromium)	$\langle w_{Cr} \rangle_{\text{ref}}^l$	30	wt.%
Reference temperature	$\langle w_C \rangle_{\text{ref}}^l$	1377	°C
Initial temperature	T_0	1395	°C
Ingot diameter		25×10^{-3}	m
Ingot length		75×10^{-3}	m
FE mesh size		10^{-3}	m
Time step	Δt	0.1	s
Convergence criterion (residual)	ε_R	10^{-6}	–
Convergence criterion (temperature)	ε_T	10^{-2}	K

Chapter 4

Macrosegregation with incompressible fluid motion

Contents

4.1	Introduction	58
4.2	Review fluid mechanics	58
4.3	VMS solver	58
4.4	Computational stability	58
4.4.1	CFL condition	58
4.4.2	Integration order	58
4.5	Application to multicomponent alloys	59
4.6	Macroscopic freckle prediction	59
4.6.1	Introduction	59
4.6.2	Experimental work	59
4.6.3	Macroscopic scale simulations	59
4.7	Meso-Macro freckle prediction	60

Chapter 4. Macrosegregation with incompressible fluid motion

this chapter discusses the following points:

- Review fluid mechanics briefly (MINI element and VMS and talk about the available solvers in Cimlib)
- Give the VMS equations referring to Hachem article
- Coupling the energy resolution from chapter 2 to fluid mechanics and solute balance
- Make a transition to speak about freckles
- Application: Ternary solidification with freckles
- Application: Macroscopic Freckle prediction: pure FE
- Application Multi-scale Freckle prediction: FE + grain structure (in which lies a part about nucleation-growth and how numerically we reach a smaller scale, the scale of the grain boundaries)

4.1 Introduction

The previous chapter covered the energy solver ...

4.2 Review fluid mechanics

Review fluid mechanics briefly (MINI element and VMS and talk about the available solvers in Cimlib)

4.3 VMS solver

Give the VMS equations referring to Hachem article + weak form + stabilization

As for the last equation in [table 2.1](#), we follow the assumption of an incompressible liquid phase, which gives:

$$\frac{\partial \langle \rho \rangle}{\partial t} = 0 \quad (4.1)$$

4.4 Computational stability

4.4.1 CFL condition

4.4.2 Integration order

Using P1 linear elements implies a P2 integration ? what are the advantages (time) and limitations ?

4.5 Application to multicomponent alloys

Here put the Fe C Cr computation results with flow and macrosegregation and freckles

In the previous chapter, we have considered a static melt upon solidification of multi-component alloy. However, in the real conditions the melt is in constant motion and knowing that the carbon and chromium solutes have lightening effects on the liquid at nominal composition, the density inversion resulting from the composition gradient in the interdendritic liquid, may cause flow instability (segregation plumes) at the solidification front. While the selected alloy is a steel, this application is also representative of directional cooling in a single crystal casting, e.g. for nickel-base superalloys [Beckermann et al. 2000]. Solidification of this class of alloys is carefully controlled so as to prevent any freckle-type defect to exist in the as-cast state. In this section, we consider the same simulation parameters defined in [table 3.3](#) as well the geometry and thermal boundary conditions previously defined in [fig. 3.7](#). Moreover, we solve the liquid momentum conservation equation, with non-slip boundary conditions on all external sides of the cylinder.

4.6 Macroscopic freckle prediction

I should maybe mention that a constant gradient in the coming simulation is a one big difference compared to the previous FeCrC simulation

4.6.1 Introduction

I have shown the results of multicomponent alloy solidification, where we saw freckles. So let me do an introduction about freckles, the need to prevent such defect from forming (superalloys, critical use in turbine blades)

4.6.2 Experimental work

Then introduce the experimental benchmark of Natalia and Sven from the article to show that there's an effort to understand, characterize and prevent if possible freckle formation. Show figures and some experimental results but quickly, no need to put many things and distract the reader

4.6.3 Macroscopic scale simulations

Introduce the FE model and algorithm then show pure FE RESULTS

Discussion

In the literature, many successful attempts have been made to predict freckles since (for example CITE fellicelli, poireau) ... until coming to kohler thesis results in 2008. These authors tackled the problem from an qualitative perspective. To our knowledge, the only close-to-quantitative work in solidification literature was done by Ramirez et al. [2003], who attempted to draw a correlation (freckling criterion) between the process parameters and the occurence of freckles, (without any size or shape constraints, i.e. any flow instability that may appear and form the smallest freckle is considered). To accomplish this, they took a number of experiments done independently by Pollock et al. [1996] and Auburtin et al. [2000] where the casting parameters vary one at a time: casting speed (R), thermal gradient (G), angle (θ) with respect to vertical orientation and nominal composition ($\langle w_0 \rangle$), giving a database for 6 different superalloys. The experimental results were compared to a modified Rayleigh number that accounts for the various parameters. It allowed them to define a threshold for freckle formation in Nickel-base superalloys, as well as Pb-Sn alloys.

They have also investigated Pb-Sn alloys, check

Other contributions by Yuan et al. [2012] and Karagadde et al. [2014] used a medium scale model to compare the simulated formation of freckles with the results obtained by Shevchenko et al. [2013] (explain a bit more) However, all simulations show common traits in their predictions: (some words about the freckle dimensions, shape, intensity). These properties do not exactly meet with the experimental observations, just like in the In-Ga experiment. We think that the hydrodynamics scale at which freckles are born, is much smaller than the FEM scale. Since the relevant physics are not solved, even the finest FE mesh will not be enough to see the exact grain boundaries. (now it is time to do transition to CAFE)

4.7 Meso-Macro freckle prediction

parachute article :)

Bibliography

[AFS 2014]

AFS (2014). *American Foundry Society: Understanding Porosity*. URL: <http://www.afsinc.org/about/content.cfm?ItemNumber=6933> (cited on page 3).

[Andersson et al. 2002]

Andersson, J.-O., Helander, T., Höglund, L., Shi, P., and Sundman, B. (2002). “Thermo-Calc & DICTRA, computational tools for materials science”. *Calphad*, 26 (2), pp. 273–312. URL: <http://www.sciencedirect.com/science/article/pii/S0364591602000378> (cited on page 53).

[Auburtin et al. 2000]

Auburtin, P., Wang, T., Cockcroft, S. L., and Mitchell, A. (2000). “Freckle formation and freckle criterion in superalloy castings”. *Metallurgical and Materials Transactions B*, 31 (4), pp. 801–811. URL: <http://link.springer.com/article/10.1007/s11663-000-0117-9> (cited on page 60).

[Beckermann 2002]

Beckermann, C. (2002). “Modelling of macrosegregation: applications and future needs”. *International Materials Reviews*, 47 (5), pp. 243–261. URL: <http://www.maneyonline.com/doi/abs/10.1179/095066002225006557> (cited on pages 5, 6).

[Beckermann et al. 1999]

Beckermann, C., Diepers, H. J., Steinbach, I., Karma, A., and Tong, X (1999). “Modeling Melt Convection in Phase-Field Simulations of Solidification”. *Journal of Computational Physics*, 154 (2), pp. 468–496. URL: <http://www.sciencedirect.com/science/article/pii/S0021999199963234> (cited on page 28).

[Beckermann et al. 2000]

Beckermann, C., Gu, J. P., and Boettinger, W. J. (2000). “Development of a freckle predictor via rayleigh number method for single-crystal nickel-base superalloy castings”. *Metallurgical and Materials Transactions A*, 31 (10), pp. 2545–2557. URL: <http://link.springer.com/article/10.1007/s11661-000-0199-7> (cited on page 59).

[Bellet et al. 2009]

Bellet, M. et al. (2009). “Call for contributions to a numerical benchmark problem for 2D columnar solidification of binary alloys”. *International Journal of Thermal Sciences*, 48 (11), pp. 2013–2016. URL: <http://www.sciencedirect.com/science/article/pii/S129007290900177X> (cited on page 38).

Bibliography

[Boettinger et al. 2002]

Boettinger, W. J., Warren, J. A., Beckermann, C., and Karma, A. (2002). "Phase-Field Simulation of Solidification1". *Annual Review of Materials Research*, 32 (1), pp. 163–194. URL: <http://dx.doi.org/10.1146/annurev.matsci.32.101901.155803> (cited on page 26).

[Brackbill et al. 1992]

Brackbill, J. U., Kothe, D. B., and Zemach, C (1992). "A continuum method for modeling surface tension". *Journal of Computational Physics*, 100 (2), pp. 335–354. URL: <http://www.sciencedirect.com/science/article/pii/002199919290240Y> (cited on page 28).

[Carozzani 2012]

Carozzani, T. (2012). "Développement d'un modèle 3D Automate Cellulaire-Éléments Finis (CAFE) parallèle pour la prédiction de structures de grains lors de la solidification d'alliages métalliques". PhD thesis. Ecole Nationale Supérieure des Mines de Paris. URL: <http://pastel.archives-ouvertes.fr/pastel-00803282> (cited on pages 9, 52).

[Carozzani et al. 2013]

Carozzani, T. et al. (2013). "Direct Simulation of a Solidification Benchmark Experiment". *Metallurgical and Materials Transactions A*, 44 (2), pp. 873–887. URL: <http://link.springer.com/article/10.1007/s11661-012-1465-1> (cited on pages 38, 52, 53).

[Chen et al. 1997]

Chen, S., Merriman, B., Osher, S., and Smereka, P. (1997). "A Simple Level Set Method for Solving Stefan Problems". *Journal of Computational Physics*, 135 (1), pp. 8–29. URL: <http://www.sciencedirect.com/science/article/pii/S0021999197957211> (cited on page 26).

[Chen 2014]

Chen, S. (2014). "Three dimensional Cellular Automaton - Finite Element (CAFE) modeling for the grain structures development in Gas Tungsten / Metal Arc Welding processes". Theses. Ecole Nationale Supérieure des Mines de Paris. URL: <https://pastel.archives-ouvertes.fr/pastel-01038028> (cited on page 26).

[Clyne et al. 1981]

Clyne, T. W. and Kurz, W. (1981). "Solute redistribution during solidification with rapid solid state diffusion". *Metallurgical Transactions A*, 12 (6), pp. 965–971. URL: <http://link.springer.com/article/10.1007/BF02643477> (cited on page 18).

[Combeau et al. 1996]

Combeau, H., Drezet, J.-M., Mo, A., and Rappaz, M. (1996). "Modeling of microsegregation in macrosegregation computations". *Metallurgical and Materials Transactions A*, 27 (8), pp. 2314–2327. URL: <http://link.springer.com/article/10.1007/BF02651886> (cited on page 18).

[Combeau et al. 2009]

Combeau, H., Založník, M., Hans, S., and Richy, P. E. (2009). "Prediction of Macrosegregation in Steel Ingots: Influence of the Motion and the Morphology of Equiaxed Grains".

Metallurgical and Materials Transactions B, 40 (3), pp. 289–304. URL: <http://link.springer.com/article/10.1007/s11663-008-9178-y> (cited on page 6).

[Courtois et al. 2014]

Courtois, M., Carin, M., Masson, P. L., Gaied, S., and Balabane, M. (2014). “A complete model of keyhole and melt pool dynamics to analyze instabilities and collapse during laser welding”. *Journal of Laser Applications*, 26 (4), p. 042001. URL: <http://scitation.aip.org/content/lia/journal/jla/26/4/10.2351/1.4886835> (cited on page 26).

[Dantzig et al. 2009]

Dantzig, J. A. and Rappaz, M. (2009). *Solidification*. EPFL Press (cited on pages 2, 14, 18, 21, 22, 43, 50).

[Darcy 1856]

Darcy, H. (1856). *Les fontaines publiques de la ville de Dijon : exposition et application des principes à suivre et des formules à employer dans les questions de distribution d'eau*. V. Dalmont (Paris). URL: <http://gallica.bnf.fr/ark:/12148/bpt6k624312> (cited on page 14).

[Desmaison et al. 2014]

Desmaison, O., Bellet, M., and Guillemot, G. (2014). “A level set approach for the simulation of the multipass hybrid laser/GMA welding process”. *Computational Materials Science*, 91, pp. 240–250. URL: <http://www.sciencedirect.com/science/article/pii/S092702561400278X> (cited on page 26).

[Digonnet et al. 2007]

Digonnet, H., Silva, L., and Coupez, T. (2007). “Cimlib: A Fully Parallel Application For Numerical Simulations Based On Components Assembly”. *AIP Conference Proceedings*. Vol. 908. AIP Publishing, pp. 269–274. URL: <http://scitation.aip.org/content/aip/proceeding/aipcp/10.1063/1.2740823> (cited on page 10).

[Dijkstra 1959]

Dijkstra, E. W. (1959). “A note on two problems in connexion with graphs”. *Numerische Mathematik*, 1 (1), pp. 269–271. URL: <http://link.springer.com/article/10.1007/BF01386390> (cited on page 35).

[DLR 2014]

DLR (2014). *ElectroMagnetic Levitation*. <http://goo.gl/e5JhiA> (cited on page 9).

[DoITPoMS 2000]

DoITPoMS (2000). *Dissemination of IT for the Promotion of Materials Science*. URL: <http://www.doitpoms.ac.uk/> (cited on page 15).

[Doré et al. 2000]

Doré, X., Combeau, H., and Rappaz, M. (2000). “Modelling of microsegregation in ternary alloys: Application to the solidification of Al–Mg–Si”. *Acta Materialia*, 48 (15), pp. 3951–3962. URL: <http://www.sciencedirect.com/science/article/pii/S1359645400001774> (cited on page 38).

Bibliography

[Du et al. 2007]

Du, Q., Eskin, D. G., and Katgerman, L. (2007). "Modeling Macrosegregation during Direct-Chill Casting of Multicomponent Aluminum Alloys". *Metallurgical and Materials Transactions A*, 38 (1), pp. 180–189. URL: <http://link.springer.com/article/10.1007/s11661-006-9042-0> (cited on page 38).

[Du et al. 2001]

Du, Q., Li, D., Li, Y., Li, R., and Zhang, P. (2001). "Simulating a double casting technique using level set method". *Computational Materials Science*, 22 (3–4), pp. 200–212. URL: <http://www.sciencedirect.com/science/article/pii/S0927025601001902> (cited on page 26).

[Easton et al. 2011]

Easton, M., Davidson, C., and StJohn, D. (2011). "Grain Morphology of As-Cast Wrought Aluminium Alloys". *Materials Transactions*, 52 (5), pp. 842–847 (cited on page 14).

[ESAB 2014]

ESAB (2014). *New Lean Duplex Steels*. URL: <http://www.esab.com/global/en/education/new-lean-duplex-steels.cfm> (cited on page 3).

[Ettrich et al. 2014]

Ettrich, J. et al. (2014). "Modelling of transient heat conduction with diffuse interface methods". *Modelling and Simulation in Materials Science and Engineering*, 22 (8), p. 085006. URL: <http://iopscience.iop.org/0965-0393/22/8/085006> (cited on page 31).

[Felicelli et al. 1991]

Felicelli, S. D., Heinrich, J. C., and Poirier, D. R. (1991). "Simulation of freckles during vertical solidification of binary alloys". *Metallurgical Transactions B*, 22 (6), pp. 847–859. URL: <http://link.springer.com/article/10.1007/BF02651162> (cited on pages 6, 15).

[Flemings 1974]

Flemings, M. C. (1974). "Solidification processing". *Metallurgical Transactions*, 5 (10), pp. 2121–2134. URL: <http://link.springer.com/article/10.1007/BF02643923> (cited on page 6).

[Flemings et al. 1967]

Flemings, M. C. and Nereo, G. E. (1967). "Macrosegregation: Part I". *Transactions of the Metallurgical Society of AIME*, 239, pp. 1449–1461 (cited on page 15).

[Flemings et al. 1968a]

Flemings, M. C., Mehrabian, R., and Nereo, G. E. (1968a). "Macrosegregation: Part II". *Transactions of the Metallurgical Society of AIME*, 242, pp. 41–49 (cited on page 15).

[Flemings et al. 1968b]

Flemings, M. C. and Nereo, G. E. (1968b). "Macrosegregation: Part III". *Transactions of the Metallurgical Society of AIME*, 242, pp. 50–55 (cited on page 15).

[Gada et al. 2009]

Gada, V. H. and Sharma, A. (2009). "On Derivation and Physical Interpretation of Level Set Method-Based Equations for Two-Phase Flow Simulations". *Numerical Heat Trans-*

- fer, Part B: Fundamentals*, 56 (4), pp. 307–322. URL: <http://dx.doi.org/10.1080/10407790903388258> (cited on page 28).
- [Gandin 2000]**
Gandin, C. A. (2000). “From constrained to unconstrained growth during directional solidification”. *Acta Materialia*, 48 (10), pp. 2483–2501. URL: <http://www.sciencedirect.com/science/article/pii/S1359645400000707> (cited on page 47).
- [Giamei et al. 1970]**
Giamei, A. F. and Kear, B. H. (1970). “On the nature of freckles in nickel base superalloys”. *Metallurgical Transactions*, 1 (8), pp. 2185–2192. URL: <http://link.springer.com/article/10.1007/BF02643434> (cited on page 6).
- [Gibou et al. 2003]**
Gibou, F., Fedkiw, R., Caflisch, R., and Osher, S. (2003). “A Level Set Approach for the Numerical Simulation of Dendritic Growth”. *Journal of Scientific Computing*, 19 (1-3), pp. 183–199. URL: <http://link.springer.com/article/10.1023/A%3A1025399807998> (cited on page 26).
- [Gouttebroze 2005]**
Gouttebroze, S. (2005). “Modélisation 3d par éléments finis de la macroségrégation lors de la solidification d’alliages binaires”. PhD thesis. École Nationale Supérieure des Mines de Paris. URL: <https://pastel.archives-ouvertes.fr/pastel-00001885/document> (cited on page 9).
- [Hachani et al. 2012]**
Hachani, L. et al. (2012). “Experimental analysis of the solidification of Sn–3 wt.%Pb alloy under natural convection”. *International Journal of Heat and Mass Transfer*, 55 (7–8), pp. 1986–1996. URL: <http://www.sciencedirect.com/science/article/pii/S0017931011007009> (cited on page 52).
- [Harlow et al. 1965]**
Harlow, F. H. and Welch, J. E. (1965). “Numerical Calculation of Time-Dependent Viscous Incompressible Flow of Fluid with Free Surface”. *Physics of Fluids (1958-1988)*, 8 (12), pp. 2182–2189. URL: <http://scitation.aip.org/content/aip/journal/pof1/8/12/10.1063/1.1761178> (cited on page 26).
- [Hebditch et al. 1974]**
Hebditch, D. J. and Hunt, J. D. (1974). “Observations of ingot macrosegregation on model systems”. *Metallurgical Transactions*, 5 (7), pp. 1557–1564. URL: <http://link.springer.com/article/10.1007/BF02646326> (cited on page 52).
- [Hirt 1971]**
Hirt, C. W. (1971). “An arbitrary Lagrangian-Eulerian computing technique”. *Proceedings of the Second International Conference on Numerical Methods in Fluid Dynamics*. Ed. by M. Holt. Lecture Notes in Physics 8. Springer Berlin Heidelberg, pp. 350–355. URL: http://link.springer.com/chapter/10.1007/3-540-05407-3_50 (cited on page 25).
- [Hirt et al. 1981]**
Hirt, C. W and Nichols, B. D (1981). “Volume of fluid (VOF) method for the dynamics of

Bibliography

free boundaries". *Journal of Computational Physics*, 39 (1), pp. 201–225. URL: <http://www.sciencedirect.com/science/article/pii/0021999181901455> (cited on page 26).

[Hysing et al. 2009]

Hysing, S. et al. (2009). "Quantitative benchmark computations of two-dimensional bubble dynamics". *International Journal for Numerical Methods in Fluids*, 60 (11), pp. 1259–1288. URL: <http://onlinelibrary.wiley.com/doi/10.1002/fld.1934/abstract> (cited on page 32).

[Karagadde et al. 2014]

Karagadde, S., Yuan, L., Shevchenko, N., Eckert, S., and Lee, P. D. (2014). "3-D microstructural model of freckle formation validated using in situ experiments". *Acta Materialia*, 79, pp. 168–180. URL: <http://www.sciencedirect.com/science/article/pii/S1359645414004984> (cited on page 60).

[Karma et al. 1996]

Karma, A. and Rappel, W.-J. (1996). "Phase-field method for computationally efficient modeling of solidification with arbitrary interface kinetics". *Physical Review E*, 53 (4), R3017–R3020. URL: <http://link.aps.org/doi/10.1103/PhysRevE.53.R3017> (cited on page 26).

[Khan et al. 2014]

Khan, M. I., Mostafa, A. O., Aljarrah, M., Essadiqi, E., and Medraj, M. (2014). "Influence of Cooling Rate on Microsegregation Behavior of Magnesium Alloys". *Journal of Materials*, 2014, e657647. URL: <http://www.hindawi.com/journals/jma/2014/657647/abs/> (cited on page 18).

[Kobayashi 1988]

Kobayashi, S. (1988). "Solute redistribution during solidification with diffusion in solid phase: A theoretical analysis". *Journal of Crystal Growth*, 88 (1), pp. 87–96. URL: <http://www.sciencedirect.com/science/article/pii/S0022024898900100> (cited on page 18).

[Lesoult 2005]

Lesoult, G. (2005). "Macrosegregation in steel strands and ingots: Characterisation, formation and consequences". *Materials Science and Engineering: A*, International Conference on Advances in Solidification Processes 413–414, pp. 19–29. URL: <http://www.sciencedirect.com/science/article/pii/S0921509305010063> (cited on page 6).

[Liu 2005]

Liu, W. (2005). "Finite Element Modelling of Macrosegregation and Thermomechanical Phenomena in Solidification Processes". PhD thesis. École Nationale Supérieure des Mines de Paris. URL: <http://pastel.archives-ouvertes.fr/pastel-00001339> (cited on page 9).

[Maitre 2006]

Maitre, E. (2006). "Review of numerical methods for free interfaces". Les Houches, France. URL: <http://goo.gl/Re6f3a> (cited on page 26).

[Martorano et al. 2003]

Martorano, M. A., Beckermann, C., and Gandin, C.-A. (2003). “A solutal interaction mechanism for the columnar-to-equiaxed transition in alloy solidification”. *Metallurgical and Materials Transactions A*, 34 (8), pp. 1657–1674. URL: <http://link.springer.com/article/10.1007/s11661-003-0311-x> (cited on page 18).

[Mesri et al. 2009]

Mesri, Y., Digonnet, H., and Coupez, T. (2009). “Advanced parallel computing in material forming with CIMLib”. *European Journal of Computational Mechanics/Revue Européenne de Mécanique Numérique*, 18 (7-8), pp. 669–694. URL: <http://www.tandfonline.com/doi/abs/10.3166/ejcm.18.669-694> (cited on page 10).

[Mosbah 2008]

Mosbah, S. (2008). “Multiple scales modeling of solidification grain structures and segregation in metallic alloys”. PhD thesis. École Nationale Supérieure des Mines de Paris. URL: <https://tel.archives-ouvertes.fr/tel-00349885/document> (cited on page 9).

[Ni et al. 1991]

Ni, J. and Beckermann, C. (1991). “A volume-averaged two-phase model for transport phenomena during solidification”. *Metallurgical Transactions B*, 22 (3), pp. 349–361. URL: <http://link.springer.com/article/10.1007/BF02651234> (cited on pages 18, 19, 21, 50).

[Osher et al. 1988]

Osher, S. and Sethian, J. A. (1988). “Fronts propagating with curvature-dependent speed: Algorithms based on Hamilton-Jacobi formulations”. *Journal of Computational Physics*, 79 (1), pp. 12–49. URL: <http://www.sciencedirect.com/science/article/pii/0021999188900022> (cited on pages 26, 27).

[Osher et al. 2003]

Osher, S. and Fedkiw, R. (2003). “Signed Distance Functions”. *Level Set Methods and Dynamic Implicit Surfaces*. Applied Mathematical Sciences 153. Springer New York, pp. 17–22. URL: http://link.springer.com/chapter/10.1007/0-387-22746-6_2 (cited on page 35).

[Peng et al. 1999]

Peng, D., Merriman, B., Osher, S., Zhao, H., and Kang, M. (1999). “A PDE-Based Fast Local Level Set Method”. *Journal of Computational Physics*, 155 (2), pp. 410–438. URL: <http://www.sciencedirect.com/science/article/pii/S0021999199963453> (cited on pages 29, 34).

[Poirier 1987]

Poirier, D. R. (1987). “Permeability for flow of interdendritic liquid in columnar-dendritic alloys”. *Metallurgical Transactions B*, 18 (1), pp. 245–255. URL: <http://link.springer.com/article/10.1007/BF02658450> (cited on page 15).

[Pollock et al. 1996]

Pollock, T. M. and Murphy, W. H. (1996). “The breakdown of single-crystal solidification in high refractory nickel-base alloys”. *Metallurgical and Materials Transactions A*, 27 (4),

Bibliography

pp. 1081–1094. URL: <http://link.springer.com/article/10.1007/BF02649777> (cited on page 60).

[Prosperetti 2002]

Prosperetti, A. (2002). “Navier-Stokes Numerical Algorithms for Free-Surface Flow Computations: An Overview”. *Drop-Surface Interactions*. Ed. by M. Rein. CISM International Centre for Mechanical Sciences 456. Springer Vienna, pp. 237–257. URL: http://link.springer.com/chapter/10.1007/978-3-7091-2594-6_8 (cited on page 26).

[Ramirez et al. 2003]

Ramirez, J. C. and Beckermann, C. (2003). “Evaluation of a rayleigh-number-based freckle criterion for Pb-Sn alloys and Ni-base superalloys”. *Metallurgical and Materials Transactions A*, 34 (7), pp. 1525–1536. URL: <http://link.springer.com/article/10.1007/s11661-003-0264-0> (cited on pages 15, 60).

[Rappaz et al. 2003]

Rappaz, M., Bellet, M., and Deville, M. (2003). *Numerical Modeling in Materials Science and Engineering*. Springer Series in Computational Mathematics. Springer Berlin Heidelberg (cited on pages 15, 19, 39, 43).

[Rivaux 2011]

Rivaux, B. (2011). “Simulation 3D éléments finis des macroségrégations en peau induites par déformations thermomécaniques lors de la solidification d’alliages métalliques”. PhD thesis. École Nationale Supérieure des Mines de Paris. URL: <http://pastel.archives-ouvertes.fr/pastel-00637168> (cited on pages 9, 19, 52).

[Sarazin et al. 1992]

Sarazin, J. R. and Hellawell, A. (1992). “Studies of Channel-Plume Convection during Solidification”. *Interactive Dynamics of Convection and Solidification*. Ed. by S. H. Davis, H. E. Huppert, U. Müller, and M. G. Worster. NATO ASI Series 219. Springer Netherlands, pp. 143–145. URL: http://link.springer.com/chapter/10.1007/978-94-011-2809-4_22 (cited on page 3).

[Schneider et al. 1997]

Schneider, M. C., Gu, J. P., Beckermann, C., Boettinger, W. J., and Kattner, U. R. (1997). “Modeling of micro- and macrosegregation and freckle formation in single-crystal nickel-base superalloy directional solidification”. *Metallurgical and Materials Transactions A*, 28 (7), pp. 1517–1531. URL: <http://link.springer.com/article/10.1007/s11661-997-0214-3> (cited on page 3).

[Sethian 1996]

Sethian, J. A. (1996). “A fast marching level set method for monotonically advancing fronts”. *Proceedings of the National Academy of Sciences*, 93 (4), pp. 1591–1595. URL: <http://www.pnas.org/content/93/4/1591> (cited on page 35).

[Shakoor et al. 2015]

Shakoor, M., Scholtes, B., Bouchard, P.-O., and Bernacki, M. (2015). “An efficient and parallel level set reinitialization method - Application to micromechanics and microstructural evolutions”. *Applied Mathematical Modelling (submitted)*, (cited on page 35).

[Shevchenko et al. 2013]

Shevchenko, N., Boden, S., Gerbeth, G., and Eckert, S. (2013). "Chimney Formation in Solidifying Ga-25wt pct In Alloys Under the Influence of Thermosolutal Melt Convection". *Metallurgical and Materials Transactions A*, 44 (8), pp. 3797–3808. URL: <http://link.springer.com/article/10.1007/s11661-013-1711-1> (cited on pages 3, 60).

[Strotos et al. 2008]

Strotos, G., Gavaises, M., Theodorakakos, A., and Bergeles, G. (2008). "Numerical investigation of the cooling effectiveness of a droplet impinging on a heated surface". *International Journal of Heat and Mass Transfer*, 51 (19–20), pp. 4728–4742. URL: <http://www.sciencedirect.com/science/article/pii/S001793100800149X> (cited on page 31).

[Süli 2000]

Süli, E. (2000). *Lecture Notes on Finite Element Methods for Partial Differential Equations* (cited on page 43).

[Sun et al. 2004]

Sun, Y. and Beckermann, C. (2004). "Diffuse interface modeling of two-phase flows based on averaging: mass and momentum equations". *Physica D: Nonlinear Phenomena*, 198 (3–4), pp. 281–308. URL: <http://www.sciencedirect.com/science/article/pii/S0167278904003689> (cited on page 28).

[Sussman et al. 1994]

Sussman, M., Smereka, P., and Osher, S. (1994). "A Level Set Approach for Computing Solutions to Incompressible Two-Phase Flow". *Journal of Computational Physics*, 114 (1), pp. 146–159. URL: <http://www.sciencedirect.com/science/article/pii/S0021999184711557> (cited on pages 32–34).

[Swaminathan. et al. 1993]

Swaminathan., C. R. and Voller, V. R. (1993). "On The Enthalpy Method". *International Journal of Numerical Methods for Heat & Fluid Flow*, 3 (3), pp. 233–244. URL: <http://www.emeraldinsight.com/journals.htm?articleid=1665561&show=abstract> (cited on page 38).

[Tan et al. 2007]

Tan, L. and Zabaras, N. (2007). "A level set simulation of dendritic solidification of multi-component alloys". *Journal of Computational Physics*, 221 (1), pp. 9–40. URL: <http://www.sciencedirect.com/science/article/pii/S0021999106002737> (cited on page 26).

[TCFE6 2010]

TCFE6 (2010). *TCFE6: a thermodynamic database for different kinds of steels and Fe-based alloys*. Stockholm, SE. URL: <http://goo.gl/qiD3kE> (cited on page 53).

[Thuin et al. 2004]

Thuinet, L. and Combeau, H. (2004). "Prediction of macrosegregation during the solidification involving a peritectic transformation for multicomponent steels". *Journal of*

Bibliography

Materials Science, 39 (24), pp. 7213–7219. URL: <http://link.springer.com/article/10.1023/B%3AJMSC.0000048734.34597.1e> (cited on page 38).

[Tiller et al. 1953]

Tiller, W. A., Jackson, K. A., Rutter, J. W., and Chalmers, B (1953). “The redistribution of solute atoms during the solidification of metals”. *Acta Metallurgica*, 1 (4), pp. 428–437. URL: <http://www.sciencedirect.com/science/article/pii/0001616053901266> (cited on page 14).

[Tourret et al. 2009]

Tourret, D. and Gandin, C. A. (2009). “A generalized segregation model for concurrent dendritic, peritectic and eutectic solidification”. *Acta Materialia*, 57 (7), pp. 2066–2079. URL: <http://www.sciencedirect.com/science/article/pii/S1359645409000184> (cited on page 18).

[Vigneaux 2007]

Vigneaux, P. (2007). “Méthodes Level Set pour des problèmes d’interface en microfluïque”. PhD thesis. Université Sciences et Technologies - Bordeaux I. URL: <https://tel.archives-ouvertes.fr/tel-00189409/document> (cited on page 34).

[Ville et al. 2011]

Ville, L., Silva, L., and Coupez, T. (2011). “Convected level set method for the numerical simulation of fluid buckling”. *International Journal for Numerical Methods in Fluids*, 66 (3), pp. 324–344. URL: <http://onlinelibrary.wiley.com/doi/10.1002/fld.2259/abstract> (cited on page 34).

[Wang et al. 1993]

Wang, C. Y. and Beckermann, C. (1993). “A multiphase solute diffusion model for dendritic alloy solidification”. *Metallurgical Transactions A*, 24 (12), pp. 2787–2802. URL: <http://link.springer.com/article/10.1007/BF02659502> (cited on page 18).

[WeldReality 2014]

WeldReality (2014). *Aluminum Alloys*. URL: <http://www.weldreality.com/aluminumalloys.htm> (cited on page 3).

[WSA 2014]

WSA (2014). *World Steel Association: Statistics archive*. URL: <http://www.worldsteel.org/statistics/statistics-archive.html> (cited on page 8).

[Xu et al. 1991]

Xu, D. and Li, Q. (1991). “Gravity- and Solidification-Shrinkage-Induced Liquid Flow in a Horizontally Solidified Alloy Ingot”. *Numerical Heat Transfer, Part A: Applications*, 20 (2), pp. 203–221. URL: <http://dx.doi.org/10.1080/10407789108944817> (cited on page 15).

[Yuan et al. 2012]

Yuan, L. and Lee, P. D. (2012). “A new mechanism for freckle initiation based on microstructural level simulation”. *Acta Materialia*, 60 (12), pp. 4917–4926. URL: <http://www.sciencedirect.com/science/article/pii/S1359645412003205> (cited on page 60).